

Master Thesis

# MODELLING SHIELDED TEMPERATURE SENSORS

AN ASSESSMENT OF THE NETATMO CITIZEN WEATHER STATION

Yann Georg Büchau

Id 6436211

Degree Programme MSc. Meteorology

1<sup>st</sup> supervisor Prof. Dr. Felix Ament

2<sup>nd</sup> supervisor Dr. Sarah Wiesner

Meteorological Institute

University of Hamburg

13<sup>th</sup> March, 2018

**Title:**

Modeling shielded temperature sensors -  
an assessment of the Netatmo private weather station network in Hamburg



# Abstract

A common challenge in urban climate research is the supply of both comprehensive and solid datasets. Resulting from high associated material and staff costs, professionally maintained meteorological measurement sites are usually only sparsely distributed. But especially in cities the need for more dense observation networks arises to study the heterogeneous urban climate and its impacts on citizen health and comfort. Crowdsourcing data from citizen weather station networks has a promising potential to fill the present data gap in urban areas. Having expanded to a decent spatial and temporal resolution, the Netatmo citizen weather station network is one of the globally most established publicly accessible meteorological crowdsourcing networks.

Unfortunately, the effective data quality of such networks is widely unknown. When considering crowdsourced data, the question inevitably emerges how to evaluate these readings. Filtering based on statistical scores and comparison to well-known high quality reference sites is a possibility to sort out strikingly conspicuous data and has been performed by several researchers before. This work addresses the data quality question in a slightly different way, taking the physical aspects of temperature measurement more into account.

The overall motivation of this work is to provide a comprehensive and robust simulation tool for analyses and assessments of Netatmo outdoor module temperature data. To accomplish this, based on the concept that every measuring apparatus underlies the laws of physics, a prognostic energy balance model for the Netatmo outdoor module is introduced. The model is deduced from the most prominent physical processes that a common temperature sensor is influenced by: thermal inertia, short- and long-wave radiation budget, heat conduction from probe casing to the actual sensor and surface latent and sensible heat fluxes. Throughout the document the model is derived in detail and calibrated using both classical experimental as well as optimization approaches.

Simulations of an exposed Netatmo outdoor module at the Wettermast Hamburg measurement site identify the solar radiation as the dominant driver of air temperature measurement deviations. Moreover, the temperature measurement seems to be influenced by the long-wave radiation budget as least as significantly as by the surrounding air temperature. This indicates that urban Netatmo outdoor module readings should rather be interpreted as a combination of the adjacent building temperature and the actual air temperature. Furthermore, deviations caused by the outdoor module's temporal lag are marginal compared to other influences.



# Contents

<b>1</b>	<b>Introduction</b>	<b>1</b>
<b>2</b>	<b>Netatmo Citizen Weather Station</b>	<b>3</b>
2.1	Indoor Module . . . . .	3
2.2	Outdoor Module . . . . .	3
2.3	Data Flow . . . . .	7
<b>3</b>	<b>Energy Balance Model</b>	<b>11</b>
3.1	Concept . . . . .	11
3.2	Equations . . . . .	12
3.3	Parametrisations . . . . .	13
3.4	Implementation . . . . .	18
<b>4</b>	<b>Calibration</b>	<b>19</b>
4.1	Condensing the Equations . . . . .	19
4.2	Optimization . . . . .	27
<b>5</b>	<b>Implications</b>	<b>33</b>
5.1	Model Setup and Forcing . . . . .	33
5.2	Reference Simulation . . . . .	33
5.3	Influence of the Radiation Budget . . . . .	34
5.4	Influence of the Outdoor Module Size . . . . .	41
<b>6</b>	<b>Conclusion</b>	<b>47</b>
<b>7</b>	<b>Outlook</b>	<b>49</b>
	<b>References</b>	<b>53</b>





# List of Figures

2.1	Netatmo devices used in this study . . . . .	4
2.2	Disassembled Netatmo outdoor module . . . . .	5
2.3	Netatmo outdoor module time constant . . . . .	6
2.4	Netatmo outdoor module sensor accuracy assessment . . . . .	8
2.5	Netatmo data flow . . . . .	9
2.6	Netatmo CWS in Hamburg . . . . .	9
3.1	Energy balance model concept . . . . .	13
4.1	Albedo determination experiment . . . . .	21
4.2	Radiation experiments . . . . .	23
4.3	Determination of the cover's heat capacity . . . . .	25
4.4	Determination of the sensor unit's heat capacity . . . . .	26
4.5	Bulk transfer coefficient experiment . . . . .	27
4.6	Bulk transfer coefficient determination . . . . .	28
4.7	Concept of model optimization . . . . .	30
4.8	Optimization results for devices GAMMA and DELTA . . . . .	31
4.9	Optimization results for devices ZETA and BETA . . . . .	32
5.1	Reference simulation - spring week . . . . .	35
5.2	Reference simulation - summer week . . . . .	36
5.3	Reference simulation - winter week . . . . .	37
5.4	Reference simulation - air and ground temperature vs. Netatmo temperature . . . . .	38
5.5	Reference simulation - mean of air and ground surface temperature . . . . .	39
5.6	Reflective cover scenario simulation . . . . .	40
5.7	Simulation with different Netatmo outdoor module sizes . . . . .	43
5.8	Simulation of an enlarged Netatmo outdoor module . . . . .	44
5.9	Simulation of a demagnified Netatmo outdoor module . . . . .	45
7.1	Inverse modelling concept . . . . .	51





# List of Tables

2.1	Netatmo outdoor module weight . . . . .	4
3.1	Model assumptions . . . . .	12
3.2	Equation symbols . . . . .	14
4.1	Simplifying scenarios . . . . .	20
4.2	Calibration results by equation construing . . . . .	29
4.3	Calibration results after optimization . . . . .	30





# Glossary

<b>API</b>	Application Programming Interface
<b>bottom plate</b>	Netatmo outdoor module's plastic bottom plate covering the sensor board from below
<b>cover</b>	Netatmo outdoor module's aluminium shell including the plastic inlet
<b>CWS</b>	citizen weather station
<b>forcing</b>	environmental conditions actively influencing the Netatmo outdoor module's temperature reading
<b>HMP</b>	VAISALA HMP155 temperature and humidity probe
<b>KT19</b>	HEITRONICS KT19 radiation pyrometer
<b>L-BFGS-B</b>	L-BFGS-B bound-constrained optimization algorithm
<b>parameter</b>	value defining the model's characteristics
<b>RMSE</b>	root mean squared error
<b>RK4</b>	Runge-Kutta-4th order numerical scheme
<b>SHT20</b>	SENSIRION SHT20 temperature and humidity sensor
<b>sensor board</b>	Netatmo outdoor module's circuitery board including the SHT20 sensor and the communication components
<b>sensor unit</b>	Netatmo outdoor module's plastic battery casing including the sensor board, the batteries and the bottom plate
<b>Wettermast HH</b>	Wettermast Hamburg measurement site
<b>Windmaster</b>	KAINDL ELECTRONIC Windmaster 2



# Chapter 1

## Introduction

Given the well-documented heterogeneity within urban areas (e.g. Eliasson and Svensson 2003; Kim and Baik 2005; Fenner et al. 2014), more dense monitoring networks are of great value for various forms of urban climate investigation (Muller et al. 2015). But building and sustaining a large-scale monitoring network with decent spatial resolution is challenging and expensive (Chapman 2015), leaving researchers partly with only a handful of meteorological measurement sites for a whole city.

The flourishing trend of the Internet/Web of Things (Gershenfeld et al. 2004; Guinard and Trifa 2009) increasingly encourages citizens to participate in public environmental measurement networks. Examples of well-established networks of this kind are the open-source SenseBox network (Bröring et al. 2011) and most notably the Netatmo citizen weather station (CWS) network. Integrating with home automation facilities, the French Netatmo company (Netatmo SAS 2018a) offers various easy to use meteorological instruments. The most basic devices are an indoor and an outdoor module measuring at least temperature and humidity. By default, the outdoor module's readings are released for public access and displayed on the company's website (Netatmo SAS 2018c). Especially in urban areas, where the population density is generally higher than in rural areas, the amount of available Netatmo data increases steadily (e.g. for the city of Berlin, Germany see Meier et al. 2017). At the time of writing there exist real-time temperature and humidity readings of well above 1,000 available Netatmo outdoor modules in the region of Hamburg, Germany. The typical distance between two adjacent stations in Hamburg is about 250 m.

The actual quality of such crowd sourced data is widely unknown (Chapman et al. 2017) and effort is being put into developing techniques to assess or increase the validity. For example Bell et al. (2015) compared measurements of several all-in-one CWSs and found significant biases for some device models. Meier et al. (2017) developed a filter for public Netatmo data in Berlin which effectively drops around half of the stations based on statistical criteria. Bruns et al. (2018) introduced a statistical method of automated quality assessment for CWSs.

All of these studies ultimately rely on statistical methods relating the data in the crowd to readings from professionally maintained sites as a reference. The downside of exclusively using statistical analyses is that the actual physical processes characterizing the measurement itself are left unregarded or in any case get heavily abstracted. This study tries to address this shortcoming by means of investigating the temperature measurement process of a Netatmo outdoor module. Given the Netatmo outdoor module's bulky and rather uncommon design for a temperature sensor, the straight-forward perception of its characteristics is a strong radiative feedback due to the anodized aluminium surface as well as a heavily lagged response. Several studies have already been conducted addressing the radiative feedback of common temperature sensors regarding their shielding (e.g. Nakamura and Mahrt 2005; Lundquist and Huggett 2008). Unfortunately, the Netatmo outdoor module's design is incompatible with the constructions examined in these studies. Furthermore, techniques to revert the lag of a slow-response sensor system have also

been thoroughly discussed before (e.g. Fofonoff et al. 1974; Horne and Toole 1980; Miloshevich et al. 2004), but only for sensor systems affected by a single forcing quantity.

Still, the Netatmo network has a major benefit - all Netatmo outdoor modules are identical in construction. So before attempting to get an understanding of the entire network's data quality, it is reasonable to first investigate its smallest component - the Netatmo outdoor module. This work focusses on the temperature measurement because temperature is on the one hand a well-documented physical quantity and on the other hand the quantity which is largely available from the Netatmo network.

The principle followed in this work is comparable to the one of simple models for the earth climate system, which have been discussed for decades (e.g. North et al. 1981; Houghton et al. 1997; Fraedrich 2001) due to their elementariness and comprehensibility. Notwithstanding, fundamental conclusions can be deduced studying these models. In this context, a prognostic energy balance model for the Netatmo outdoor module's temperature measurement is introduced in this study. The model is based on the most typical processes influencing a temperature probe: thermal inertia, short- and long-wave radiation budget, heat conduction from probe casing to the actual sensor as well as latent and sensible heat flux. The model enables to simulate what a Netatmo outdoor module would gauge given certain environmental conditions. Evidently, it also opens up general possibilities of model application like inverse modelling, e.g. for forcing retracing.

This work is structured as follows: The Netatmo outdoor module device and its characteristics are introduced in Chapter 2. The energy balance model is derived in detail in Chapter 3 along with the used equations and parametrisations. Chapter 4 then elaborates on the different calibration methods applied to determine and fine-tune the model parameters. Chapter 5 briefly demonstrates the application use-cases of the model: The temperature measurement of a Netatmo outdoor module is simulated and evaluated at the Wettermast Hamburg measurement site for different conceptual scenarios. Chapter 6 summarizes the findings and Chapter 7 elaborates on further possible model improvements.

## Chapter 2

# Netatmo Citizen Weather Station

Netatmo is a French company producing consumer-friendly weather stations that can easily be set up and which require a minimum amount of maintenance. The base package consists of an indoor and an outdoor module, both measuring at least temperature and humidity. The data recorded by the outdoor module is published by default, but the user can disable the publishing at any time. It is also possible to add other purchasable modules - e.g. a rain and a wind module - but these modules have a smaller distribution.

For this study, seven pairs of Netatmo indoor and outdoor modules were used. To ease recognition they were named according to the Greek alphabet: ALPHA, BETA, GAMMA, DELTA, EPSILON, ZETA and ETA (Figure 2.1). In the following sections both module types are introduced with a special focus on the outdoor module and its basic measurement characteristics. Additionally, the slightly complex data flow and the data acquisition possibilities are clarified to outline the potentials and limits for performing calibration experiments.

### 2.1 Indoor Module

An indoor module is the base station for other Netatmo modules like the outdoor module. It is powered via a USB cable. The indoor module measures meteorological and air quality parameters itself: temperature (accuracy according to the manufacturer Netatmo SAS (2018a):  $\pm 0.3$  K), humidity ( $\pm 3$  %), pressure ( $\pm 1$  mbar), CO<sub>2</sub> ( $\pm 50$  ppm) and noise. The pressure measurement of the indoor module is the only quantity that is made publicly available. As the maximum signal range between indoor module and outdoor module is 100 m according to the manufacturer, the pressure reading may be used as forcing input for the model later on and is comprehensibly assumed to be correct for the present study.

### 2.2 Outdoor Module

The battery-powered outdoor module is intended to be placed outside. The manual contains very rudimentary visual instructions on the right positioning. It advises to place the module in a spot that is protected from direct solar irradiation and rain. However, the station's owner is still free to decide the location wherever the measurement is intended, e.g. indoors (Meier et al. 2015).

The outdoor module measures temperature (accuracy according to manufacturer:  $\pm 0.3$  K) and humidity ( $\pm 3$  %). If the default option is left enabled, the outdoor module's data is publicly available via the Netatmo Application Programming Interface (API) as explained below. For the devices used in this study, this option was disabled for the experiments.

The outdoor module consists of two main components as shown in Figure 2.2a: firstly, a shell consisting mostly of aluminium (further called the 'cover') - and secondly the part containing the actual electrical components (further called the 'sensor unit'). But the module can be further

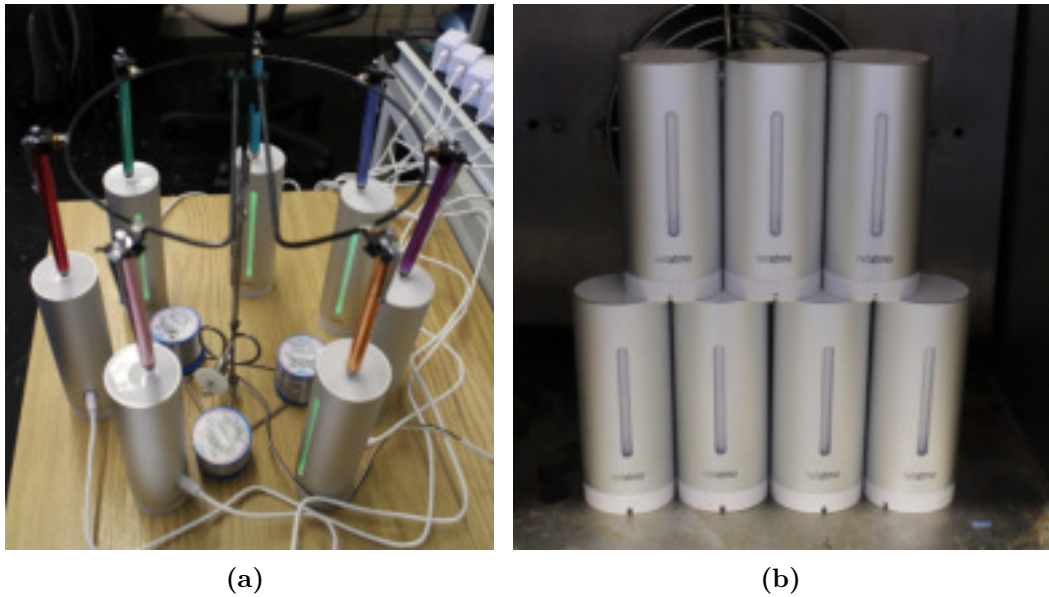


**Figure 2.1:** Netatmo devices used in this study: The battery-powered frame in (a) touches the seven Netatmo indoor modules with touchpens at a frequency of around 15 seconds. (b) Seven corresponding Netatmo outdoor modules in the climate chamber.

**Table 2.1:** Weight of the Netatmo outdoor modules in use, batteries included

	<u>Mean</u>
outdoor module	$144.80 \pm 0.86$ g
cover	$81.80 \pm 0.78$ g
sensor unit	$63.00 \pm 0.21$ g

disassembled as shown in detail in Figure 2.2b. A combined temperature and humidity sensor chip (SHT20, Sensirion 2014) is soldered onto the circuitry board, which will subsequently be referred to as ‘sensor board’ (Figure 2.2d). The module as a whole weighs around 145 g, whereby the cover is slightly heavier than the sensor unit (Table 2.1).

In the following the outdoor module’s basic measurement characteristics are assessed experimentally. The outdoor module’s temporal lag behaviour is investigated and the accuracy of the built-in SHT20 sensor chip is examined.

### Temporal Lag Behaviour

Most studies on crowdsourced data mainly focus on the devices’ stationary accuracy (Bell et al. 2015; Chapman et al. 2017; Meier et al. 2017) and neglect the temporal component, i.e. the lag behaviour, introduced by ‘design flaws’ as Bell et al. (2015) put it. Since CWSs are commercial products they also need to have an appealing design. The Netatmo CWS is a good example - while being visually appealing, the radiation properties of the outdoor module’s cover

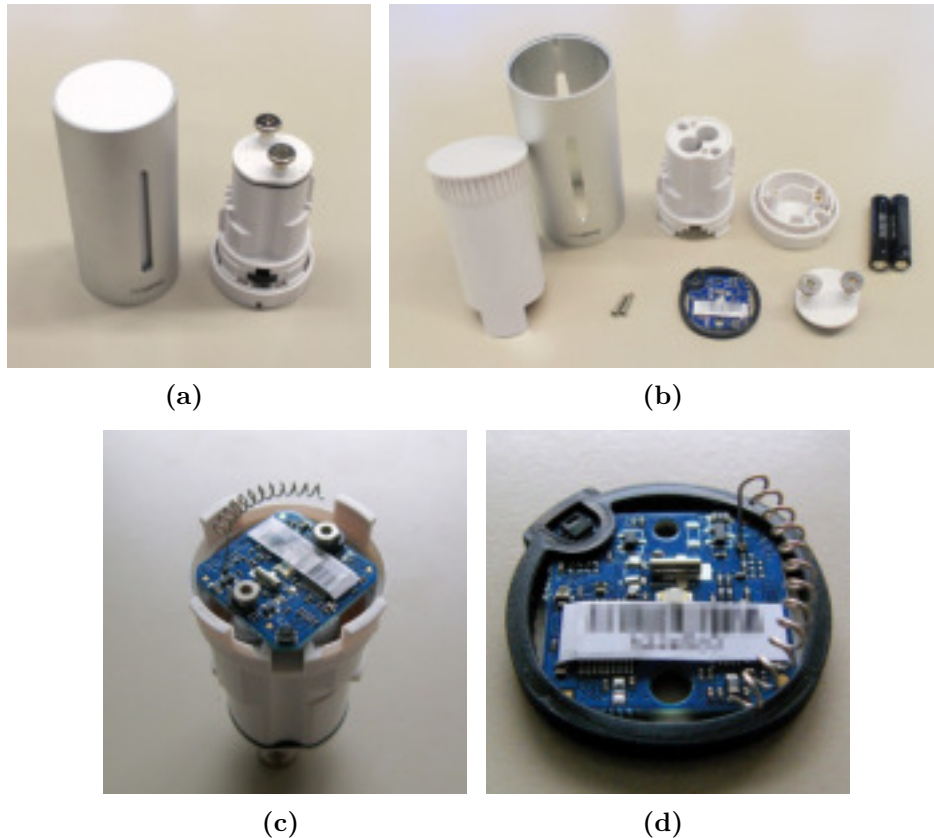


**Figure 2.2:** Disassembled Netatmo outdoor module. (a) cover and sensor unit as main parts of the outdoor module, (b) top row: cylindrical aluminium shell, battery casing, bottom plate, batteries - bottom row: plastic shell inlet, screws, sensor board, battery cap, (c) upside down - board visible, setup for the sensor accuracy experiment, (d) sensor board with the SHT20 sensor in the top left-hand corner.

seem only questionably appropriate. Furthermore, the SHT20 temperature and humidity sensor is very concealed within the outdoor module, which increases its response time.

To quantify this, the seven Netatmo modules were heated up (cooled down) in the climate chamber on a grid. Experiments were conducted both with and without the cover. After stationarity was achieved, the outdoor modules were put in a calm, dark place to adjust to the environmental temperature. A non-linear least squares fit of an exponential decay function to the obtained temperature data was then used to determine the time constant of each outdoor module (Figure 2.3).

It turns out, that under calm conditions the outdoor module has a quite large time constant of more than 20 minutes. Without the cover the time constant decreases slightly to approximately 15 minutes. Since the time constant is defined as the time until an initial perturbation is lessened to a fraction of  $\frac{1}{e} \approx 37\%$ , the outdoor module's actual wind-less adjustment time is roughly one hour for an instantaneous significant change in the environmental temperature. Meier et al. (2017) also asserted during their Netatmo outdoor module calibration experiments that an adjustment period of up to two hours was necessary. This surprisingly large lag comprehensibly raises concerns about the Netatmo network's data quality and will be assessed throughout this study.

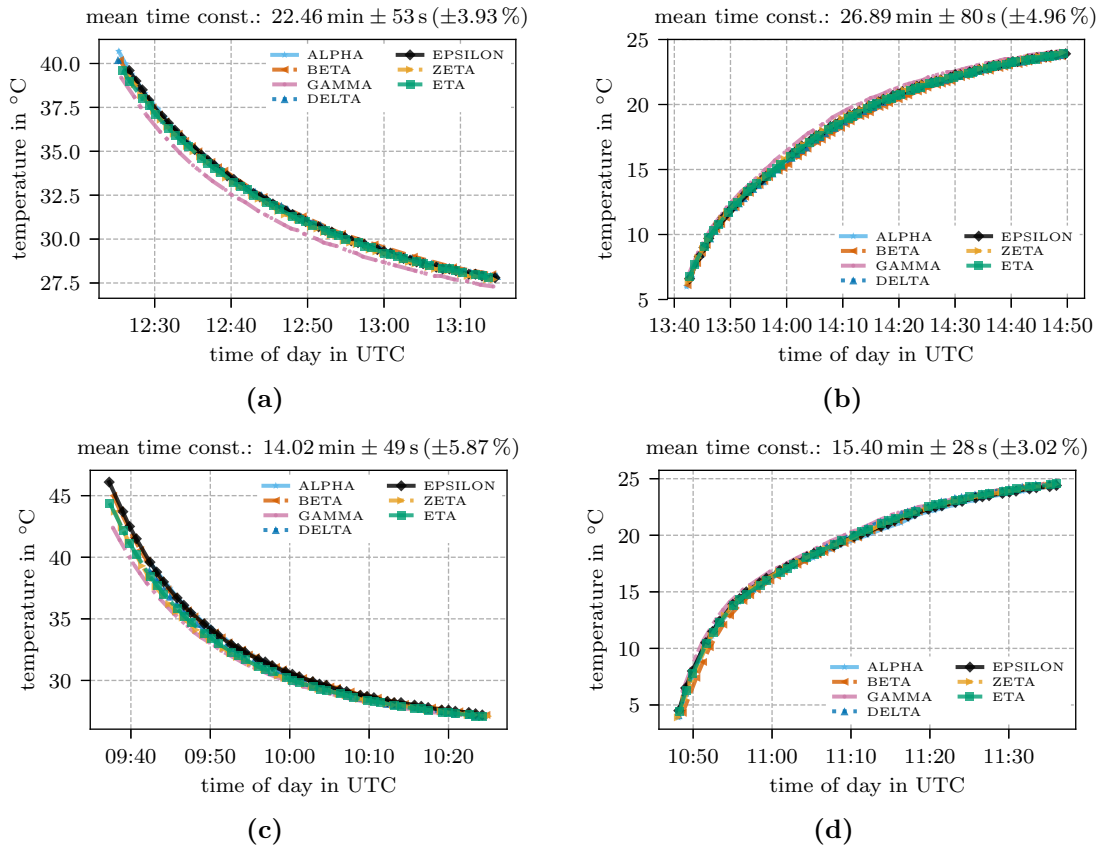


**Figure 2.3:** Netatmo outdoor module time constant cooldown and warmup experiment results with the cover (a and b) and without (c and d) under calm conditions. The time constants were determined using a non-linear least squares fit of an exponential decay function to the data.

A lag-correction can be formulated as the inverse of a convolution or comparable methods (Fonoff et al. 1974; Horne and Toole 1980; Miloshevich et al. 2004), as can be read about in common text books like Haddad and Parsons (1991). However, inversion of a convolution always requires the knowledge of the convolution kernel. In simple cases, the kernel can be determined via calibration experiments. But if the kernel is time dependent, i.e. the instrument’s lag behaviour is not constant in time, the lag correction becomes a matter of estimating the kernel’s time-dependency empirically. As the Netatmo outdoor module’s lag characteristics are obviously time-dependent due to the fluctuating radiative input for example, a deconvolution is thus an inappropriate correction mechanism in this case.

### Sensor Accuracy

To assess the accuracy of the SHT20 sensor chip itself, readings were compared to a VAISALA HMP155 temperature and humidity probe (HMP). An assessment of the Netatmo outdoor module’s accuracy has already been performed by Meier et al. (2017), but using only seven discrete temperature levels. The module’s slow response introduces long adjustment times which makes a continuous calibration generally challenging. As climate chambers are usually controlled electronically and don’t have a continuously adjustable thermal unit, the temperature cannot be

held exactly constant. Instead, the thermal unit is switched on and off following a hysteresis to minimize wearing of electrical switching components, resulting in a jigsaw-shaped temporal temperature pattern. A fast sensor like the HMP is able to catch these temperature variations. The climate chamber used in these experiments switches at a frequency of around one minute. Since the outdoor module in its normally assembled state has a time constant of more than 20 minutes, calibrating lagged Netatmo readings against any reference sensor that has a different time constant is non-trivial.

To address this, first the cover and the bottom plate were removed (Figure 2.2c) so that the sensor is completely exposed. All seven outdoor modules were then placed into the insulated climate chamber in a circular formation alongside the HMP. It is to be noted that, due to the design of the climate chamber, it was not possible to position the HMP within an equal distance to all Netatmo outdoor modules. To increase the temperature homogeneity in the climate chamber, a small ventilating fan was placed in the center of all devices. Two experiments were conducted - each time, the climate chamber was set to a fixed temperature until all devices had a constant reading. The climate chamber's thermal unit was then switched off and the setup was left untouched over night. Due to the climate chamber's insulation a slow adjustment to the environmental temperature was achieved. Thus, comparable and continuous time series of Netatmo sensors and the reference sensor were obtained. The results are shown in Figure 2.4.

Conspicuously, the devices ALPHA, GAMMA and ETA bear the highest resemblance to the reference sensor's readings. They were amongst the closest to the reference sensor and positioned at the climate chamber's door, which obviously has a better insulation than the other sides. Nevertheless, for the tested temperature range of around 18 °C to 42 °C the temperature sensor's accuracy primarily lies within the specification's accuracy of  $\pm 0.3$  K.

## 2.3 Data Flow

The Netatmo readings are not collected actively by the user. The whole data flow process is automated but requires an initial setup. The outdoor module communicates its readings cordlessly to the indoor module. It is not intended to intercept and readout the data at this point. Instead, the indoor module uploads the received data along with its own readings to the Netatmo cloud via a local wireless network on a five minute schedule (Figure 2.5). There is no official way to retrieve the data from within the local network directly. Instead, to obtain the data of a Netatmo station, one has to query the Netatmo API and download the data.

However, it is possible to initiate a measurement actively by touching the top of the indoor module. To increase the reading frequency for the calibration experiments, a device was built that tips touchpens onto the indoor modules' tops periodically at a frequency of around 15 seconds to instigate a measurement (Figure 2.1a). Nevertheless, the effective maximum reading frequency uploaded to the server is still roughly one minute, which is the temporal resolution limit.

### Netatmo API

The public data in the Netatmo network can be obtained through the Netatmo API (Netatmo SAS 2018b). To properly access this API, a Python package was developed (Büchau 2017b) and made publicly available. At the time of writing, there were two relevant API entry points for this work's purpose: the `Getpublicdata` method and the `Getmeasure` method.

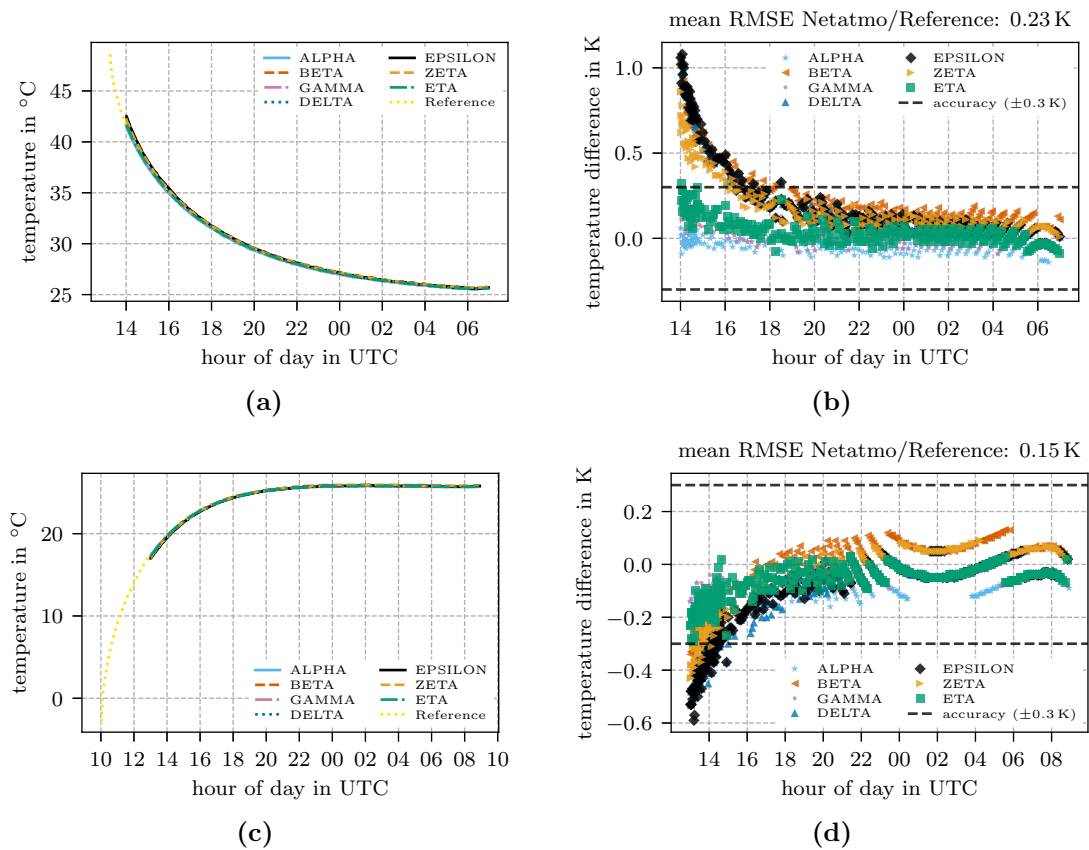


**Figure 2.4:** Qualitative assessment of the Netatmo outdoor module’s sensor accuracy. Results of the (a) cooldown and (c) warmup experiment along with the corresponding temperature differences between the Netatmo outdoor module and the HMP reference sensor reading (b and d). The SHT20 sensor chip was fully exposed during this experiment (Figure 2.2c). Netatmo outdoor module ALPHA was closest to the reference sensor. The ‘accuracy’ refers to the manufacturer’s guaranteed accuracy.

The `Getpublicdata` method can be used to obtain current public data in a specified lat/lon region and effectively yields a snapshot of present readings. However, it also contains the information, what outdoor module belongs to which indoor module. This is necessary metadata for the `Getmeasure` method. A compiled result of multiple `Getpublicdata` requests for the region of Hamburg is shown in Figure 2.6 .

The `Getmeasure` method enables acquiring past data from a single station one has access to. This may be any public station or a station one owns. To acquire timeseries data of an outdoor module, knowledge of its corresponding indoor module’s device id is needed. This id can be obtained with the `Getpublicdata` method if unknown. The `Getmeasure` method is thus the suitable API entry point for calibration and simulation purposes used further on throughout this study.

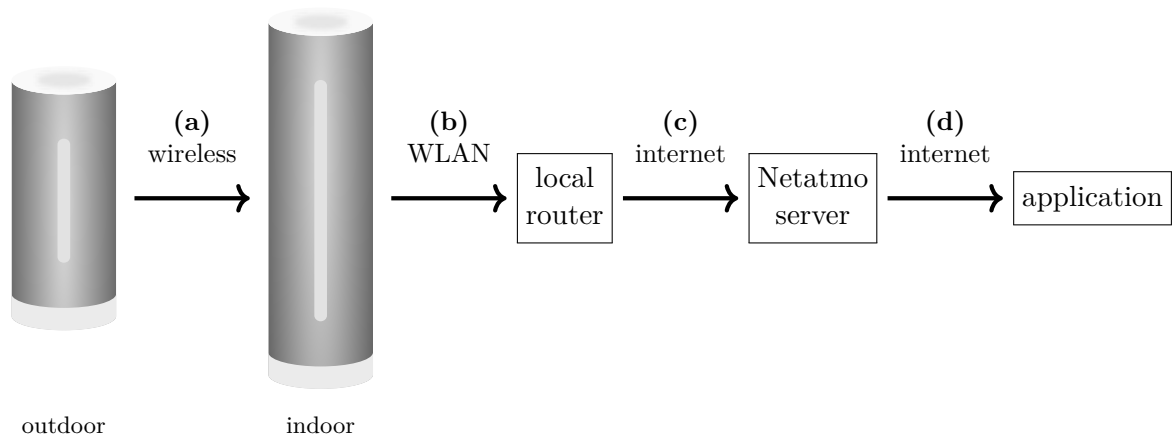


**Figure 2.5:** Data flow from outdoor module to application. The outdoor module sends its readings wirelessly to the indoor module (a) which uploads it over the local wireless network (b) to the Netatmo server (c) from where an application can retrieve it (d).

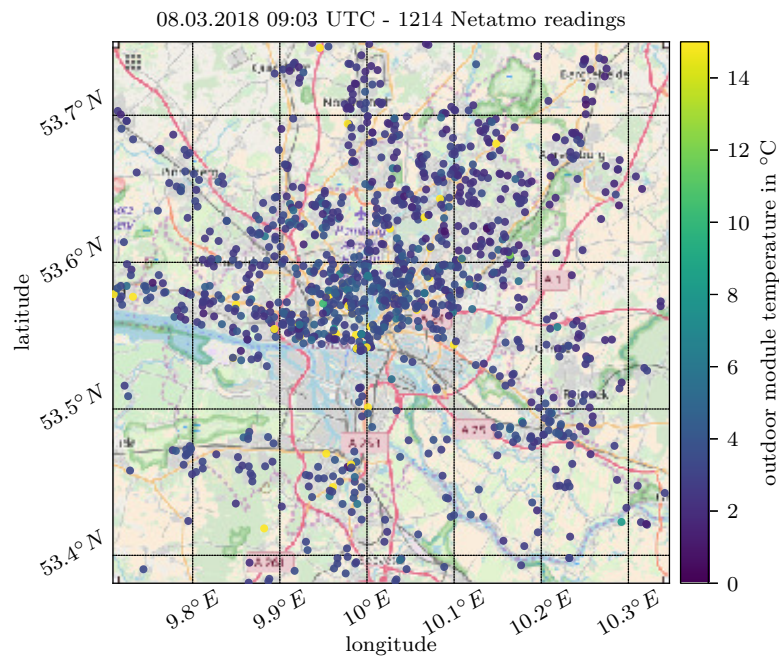


**Figure 2.6:** Snapshot of Netatmo citizen weather station temperature readings in the region of Hamburg.



# Chapter 3

## Energy Balance Model

To quantify the aforementioned considerations concerning the outdoor module's suitability as a temperature sensor, a prognostic energy balance model is now introduced and derived. This model allows for modelling what an outdoor module would gauge given a certain forcing, i.e. certain environmental conditions.

Analogously to the principle followed for simple earth climate system models, keeping the energy balance model for the outdoor module simple while maintaining representativeness was the priority during its development. It is derived with the objective that essentially any temperature measuring instrument with a similar construction as the outdoor module will be analogically modellable in principle. The parameters, i.e. the quantities defining the model's characteristics, still remain device-specific but should be equally determinable as for the Netatmo outdoor module as described in Chapter 4.

### 3.1 Concept

To keep the model's complexity low, several simplifying assumptions are made (Table 3.1). First, the outdoor module is assumed to consist of two heat reservoirs: the cover which fully encloses the sensor unit (Table 3.1I). These two reservoirs are connected solely via heat conduction (Table 3.1II). Only the cover is assumed to be exposed to the environment (Table 3.1III). As for the radiation processes, the cover's surface is supposed to be under the influence of incoming short-wave and long-wave radiation. It emits long-wave radiation itself. Furthermore, to facilitate modelling both reservoirs effectively as zero-dimensional (Table 3.1IV), all forcing is assumed to interfere homogeneously with the cover. The only quantity which obviously violates this assumption significantly in reality is the incoming short-wave radiation. Thus, this quantity needs to be transformed accordingly.

The Netatmo outdoor module is assumed to stand on a surface instead of being attached to a wall (Table 3.1V). Moreover, it is supposed that the bottom plate acts as an insulator to the ground, so no heat is exchanged at the bottom of the outdoor module (Table 3.1VI). Given the fact that the sensor board is located directly above the bottom plate (Figure 2.2c), neglecting the heat conduction to and from the placing surface will introduce an error. Nevertheless, this approach is necessary because the placing surface's temperature is difficult to parametrise in this case.

All heat fluxes are parametrised using a first order closure approach (Table 3.1VII), i.e. all heat fluxes are assumed to relate proportionally to their inducing physical quantity's gradient. For heat fluxes acting on the cover surface, a proportionality to the wind velocity is assumed (Table 3.1VIII). This implies that surface heat fluxes under calm conditions are neglected. This assumption should be safe to make as long as there is enough ventilation through wind. Eventually, it is assumed that there is no feedback from the outdoor module to the environ-

**Table 3.1:** Model assumptions

Nr.	Assumption
I	The Netatmo outdoor module consists of two heat reservoirs: the cover which fully encloses the sensor unit.
II	The cover and the sensor unit are connected solely by heat conduction.
III	The cover's surface is under the influence of incoming short- and long-wave radiation as well as sensible and latent heat flux. It emits long-wave radiation itself.
IV	The cover and the sensor unit each have no spatial temperature differences, i.e. they are both effectively treated as zero-dimensional.
V	The Netatmo outdoor module is standing on the ground, i.e. the bottom plate has no air contact from below.
VI	There is no heat flux at the bottom of the Netatmo outdoor module, i.e. the bottom plate acts as an insulator.
VII	First order heat flux closure: heat fluxes are proportional to the gradient.
VIII	Sensible and latent heat flux are proportional to the wind velocity.
IX	Bulk transfer coefficients of heat and moisture are equal.
X	There is no feedback to the environment. The device is reacting passively to the environmental conditions.

ment (Table 3.1X). The outdoor module is thus reacting passively to the environmental conditions. This assumption should again be safe to make as long as there is enough advection, i.e. enough ventilation through wind.

## 3.2 Equations

Given the aforementioned simplifying assumptions, equations describing the outdoor module's energy budget can be derived. Symbols used in the following equations are listed in Table 3.2. A schematic graph of the modelled heat fluxes is shown in Figure 3.1. The general energy balance equation for the cover's surface can then be formulated as

$$\underbrace{C_s \frac{dT_s}{dt}}_{\text{thermal inertia}} = \underbrace{-LW_{\text{out}}}_{\text{long-wave out}} + \underbrace{+LW_{\text{in}}}_{\text{long-wave in}} + \underbrace{+SW_{\text{in}}}_{\text{short-wave in}} + \underbrace{+H_S}_{\text{sensible heat flux}} + \underbrace{+H_L}_{\text{latent heat flux}} - \underbrace{\Delta H_I}_{\text{internal heat conduction}} \quad (3.1)$$

As cover and sensor unit are solely connected by heat conduction (Table 3.1II), the internal heat conduction  $\Delta H_I$  is the only process influencing the sensor unit's temperature. Thus, the energy

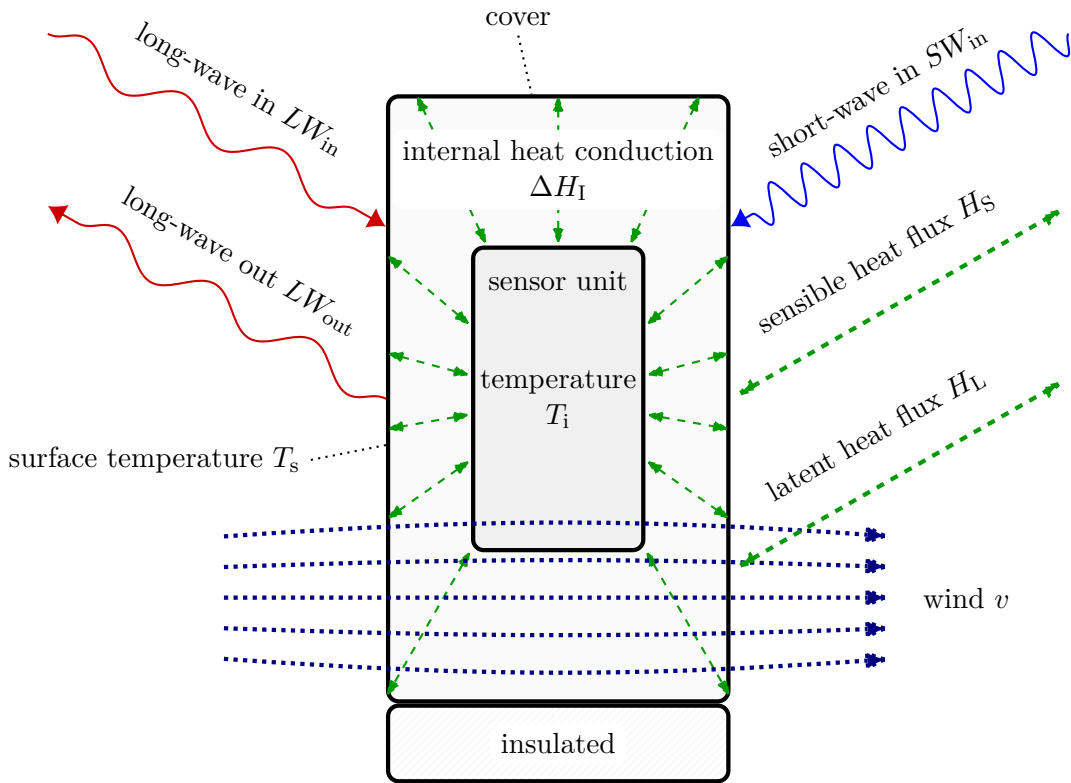


**Figure 3.1:** Energy balance model concept graph.

balance equation for the sensor unit is

$$\underbrace{C_m \frac{dT_i}{dt}}_{\text{sensor unit thermal inertia}} = \underbrace{\Delta H_I}_{\text{internal heat conduction}} \quad (3.2)$$

### 3.3 Parametrisations

In the following sections the parametrisations applied to quantify the terms in Equation 3.1 and Equation 3.2 are introduced.

#### Sensor Calibration

As asserted in Section 2.2, the temperature sensor itself seems to be accurate enough to justify the assumption that the real sensor unit temperature  $T_i$  is sufficiently represented by the measured temperature  $T_m$ :

$$T_i = T_m \quad (3.3)$$

**Table 3.2:** Symbols used in the energy balance equations

## (a) state variables

Symbol	Unit	Description
$T_s$	K	(surface) temperature of the cover
$T_i$	K	real temperature of the sensor unit

## (b) parameters

$d_m$	m	Netatmo outdoor module diameter
$h_m$	m	Netatmo outdoor module height
$w_{lw}$	1	share of sky and ground long-wave radiation
$\lambda$	W/(K m)	effective internal conductivity
$\alpha_s$	1	cover short-wave albedo
$\varepsilon_s$	1	cover long-wave emissivity
$C_s$	J/K	effective cover heat capacity
$C_m$	J/K	effective sensor unit heat capacity
$\eta$	1	bulk transfer parameter for heat and moisture

## (c) forcing

$a_{wet}$	1	wet area fraction on the cover
$T_a$	K	surrounding air temperature
$T_g$	K	ground surface temperature
$\rho_a$	kg/m <sup>3</sup>	surrounding air density
$q_a$	kg/kg	specific humidity of surrounding air
$v$	m/s	wind velocity
$I_{lw,sky}$	W/m <sup>2</sup>	total incoming sky long-wave radiation
$I_{sw}$	W/m <sup>2</sup>	total incoming short-wave radiation

## (d) physical constants

$L$	J/kg	enthalpy of vaporization of water
$c_p$	J/(kg K)	specific heat capacity of dry air under constant pressure

## (e) other

$I_{win}$	W/m <sup>2</sup>	effective incoming long-wave radiation
$q_s$	kg/kg	specific humidity in immediate proximity of the cover
$q^*$	kg/kg	saturation specific humidity
$A_s$	m <sup>2</sup>	exposed surface area of Netatmo outdoor module
$A_r$	m <sup>2</sup>	radiation receiving surface area of Netatmo outdoor module
$T_m$	K	Netatmo outdoor module's measured temperature

### Exposed Surface Area $A_s$

For the surface processes, the exposed surface area  $A_s$  needs to be determined. This can be done by a simple cylinder geometry using the outdoor module's height  $h_m$  and diameter  $d_m$ :

$$A_s = \underbrace{\pi \left( \frac{d_m}{2} \right)^2}_{\text{top area}} + \underbrace{\pi d_m h_m}_{\text{mantle area}} \quad (3.4)$$

Although the bottom plate is assumed to be an insulator (Table 3.1VI), its exposed side area should still be included because in reality it contributes to the radiation budget as well.

### Emitted Long-Wave Radiation $LW_{\text{out}}$

The emitted long-wave radiation is parametrized by the STEFAN-BOLTZMANN-law with the surface's long-wave emissivity  $\varepsilon_s$ :

$$LW_{\text{out}} = \underbrace{\varepsilon_s \sigma A_s T_s^4}_{\text{emitted long-wave radiation}} \quad (3.5)$$

As the whole exposed surface emits long-wave radiation, the exposed surface area  $A_s$  is used.

### Incoming Long-Wave Radiation $LW_{\text{in}}$

Parametrising the incoming long-wave radiation is challenging. Theoretically it depends both on global and on local incoming long-wave radiation. While global long-wave radiation is parametrizable via larger-scale pyrgeometer measurements (e.g. Wettermast Hamburg measurement site for the region of Hamburg, Brümmer et al. 2012), the local effect of buildings or other objects near the outdoor module is difficult to quantify. Still, the long-wave radiation originating from the surrounding ground surface is likely to be even greater than the sky's long-wave radiation. Thus, the effective total incoming long-wave radiation  $I_{lw,in}$  is parametrised as a weighted average of sky  $I_{lw,sky}$  and ground surface long-wave radiation which is parametrised as the blackbody radiation of the ground surface temperature  $T_g$  according to the STEFAN-BOLTZMANN-law. The weight  $0 \leq w_{lw} \leq 1$  is assumed to be  $w_{lw} = 0.5$  but keeping it adjustable makes simulating some scenarios easier. All incoming long-wave radiation is assumed to take effect on the whole exposed surface area  $A_s$ :

$$LW_{\text{in}} = \varepsilon_s I_{lw,in} A_s = \underbrace{\varepsilon_s [(1 - w_{lw}) \sigma T_g^4 + w_{lw} I_{lw,sky}]}_{\text{absorbed long-wave radiation}} A_s \quad (3.6)$$

### Incoming Short-Wave Radiation $SW_{\text{in}}$

For the incoming short-wave radiation, it is difficult to estimate the local shadowing as well as the different influence of direct and diffuse solar input. The incoming solar radiation  $I_{sw}$  is assumed to act on a receiving area  $A_r$ . This is the area affected by direct solar radiation which is

intrinsically dependent on the solar altitude. However, for simplicity, this dependency is neglected and the area is parametrised as

$$A_r = \underbrace{d_m h_m}_{\text{shadowing area}} \quad (3.7)$$

Short-wave input is then parametrised in terms of total incoming solar radiation  $I_{sw}$  acting on the receiving surface area  $A_r$ , diminished by reflection:

$$\underbrace{SW_{in}}_{\text{short-wave in}} = \underbrace{(1 - \alpha_s) A_r I_{sw}}_{\text{absorbed solar input}} \quad (3.8)$$

with  $0 < \alpha_s < 1$  being the surface albedo.

### Sensible Heat Flux $H_S$

The sensible heat flux between a surface and its surrounding air is commonly parametrised proportionally on their temperature difference, air density  $\rho_a$ , the wind velocity  $v$  and the affected area (cf. text books like Wallace and Hobbs 2006). Obeying assumption Table 3.1VIII, the same approach is taken here, appending a heat flux parameter  $\eta$  for adjustment and using the outdoor module's exposed surface area  $A_s$ :

$$H_S = \underbrace{-\rho_a c_p (T_s - T_a) A_s \eta v}_{\text{sensible heat flux}} \quad (3.9)$$

This parametrisation implies that under calm conditions the outdoor module is thermally completely decoupled from the surrounding air. Considering the time constant determination experiment (Figure 2.3), which was conducted under calm conditions, this implication seems to be only questionably fulfilled in reality. Nonetheless, assuming that thoroughly calm conditions occur only infrequently (e.g. Brümmer et al. 2012; Gryning et al. 2014), neglecting the sensible heat flux under calm conditions is a simplification that eases model calibration substantially (Chapter 4).

### Latent Heat Flux $H_L$

Analogously to the sensible heat flux the latent heat flux is usually parametrised based on the difference in humidity at the surface ( $q_s$ ) and the surrounding air ( $q_a$ ):

$$H_L = \underbrace{-\rho_a L (q_s - q_a) A_s \eta v}_{\text{general latent heat flux}} \quad (3.10)$$

For both the sensible and the latent heat flux the same parameter  $\eta$  is used (see Table 3.1IX, Wallace and Hobbs 2006). The simplest approach to quantify the specific humidity in immediate proximity of the outdoor module  $q_s$  is to establish that the outdoor module is either always dry ( $q_s = 0$ , effectively disabling the latent heat flux) or completely damp. If the entire exposed surface was covered with a liquid water film, the air in immediate proximity could be assumed

to be saturated ( $q_s = q^*(T_s)$ ). However, attempts to moisturise the entire cover surface were unsuccessful. Since the aluminium shell has a vertical orientation, most water drops run off. Only the plastic horizontal top plate is able to hold a more significant amount of liquid water. But given the fact that the outdoor module's top is farthest to the sensor, it is most likely the least significant area to influence the sensor unit's temperature. Thus,  $q_s$  is parametrized as an interpolation between the humidity of the surrounding air  $q_a$  and the saturation humidity at surface temperature  $q^*(T_s)$  depending on the cover's wet area coverage  $0 \leq a_{\text{wet}} \leq 1$ :

$$q_s = q_a + a_{\text{wet}} [q^*(T_s) - q_a] \quad (3.11)$$

With this approach Equation 3.10 is changed to

$$\underbrace{H_L}_{\text{latent heat flux}} = \underbrace{-a_{\text{wet}} \rho_a L (q^*(T_s) - q_a) A_s \eta v}_{\text{latent heat flux on partially wet surface}} \quad (3.12)$$

With  $q^*(T_s)$  and  $q_a$  being independent of each other, this parametrisation also includes condensation on the cover's surface as a warming process if  $a_{\text{wet}} > 0$ .

### Internal Heat Conduction $\Delta H_I$

The coupling of cover and sensor unit is realised by heat conduction as codified in Table 3.III. Technically, except for the fastening ring (around 1 cm in height, level with the sensor board), cover and sensor unit are separated by air and have no direct contact. However, expecting no airflow in this gap, an effective heat conduction should describe the heat transfer in between well enough. Both reservoirs include this heat transfer in their balance equations. It is parametrised as the heat conduction through an imaginary area half the size of the exposed surface area  $A_s$  and along a distance half the module's diameter  $d_m$  with an internal conductivity  $\lambda$ :

$$\Delta H_I = \underbrace{\lambda \frac{A_s}{d_m} (T_s - T_i)}_{\text{inward heat conduction}} \quad (3.13)$$

### Final Parametrized Energy Balance Equations

The final parametrized cover energy balance equation is:

$$\underbrace{\frac{C_s}{A_s} \frac{dT_s}{dt}}_{\text{thermal inertia}} = \underbrace{-\varepsilon_s \sigma T_s^4}_{\text{long-wave out}} + \underbrace{+\varepsilon_s [(1 - w_{\text{lw}}) \sigma T_g^4 + w_{\text{lw}} I_{\text{lw,sky}}]}_{\text{long-wave in}} + \underbrace{+(1 - \alpha_s) \frac{A_r}{A_s} I_{\text{sw}}}_{\text{short-wave in}} \quad (3.14)$$

$$\underbrace{-\rho_a c_p (T_s - T_a) \eta v}_{\text{sensible heat flux}} + \underbrace{-a_{\text{wet}} \rho_a L (q^*(T_s) - q_a) \eta v}_{\text{latent heat flux}} + \underbrace{-\frac{\lambda}{d_m} (T_s - T_i)}_{\text{internal heat conduction}}$$

The final parametrized sensor unit energy balance equation is:

$$\underbrace{\frac{C_m}{A_s} \frac{dT_i}{dt}}_{\text{thermal inertia}} = \underbrace{\frac{\lambda}{d_m}}_{\text{internal heat conduction}} (T_s - T_i) \quad (3.15)$$

### 3.4 Implementation

To implement this energy balance model, a Python package was developed (Büchau 2017a) and made publicly available. As Equation 3.14 is heavily non-linear due to the fourth power in the emitted long-wave radiation term and the exponential saturation humidity  $q^*(T_s)$ , it is solved with the Runge-Kutta-4th order numerical scheme (RK4) after Dormand and Prince (1980). Equation 3.15 is linear and could be solved reliably with either the implicit scheme or the RK4 as well. But as it is not possible to integrate a set of numerical schemes where all equations depend on future time steps of each other - which is the case here - the internal energy balance equation is solved with a simple explicit scheme. The forcing is fed into the model without any modification, no data assimilation technique is used. All model data is interpolated linearly if necessary.

# Chapter 4

## Calibration

The parametrisations established in Section 3.3 introduce unknown parameters (Table 3.2b) that need to be determined or estimated in order to run the model. Two calibration techniques - equation condensing and optimization - are introduced in the following, both based on experimental data.

### 4.1 Condensing the Equations

One common model calibration approach is to elaborate under which experimentally contrivable conditions the model equations boil down to a simple relationship that allows the calculation of one or more parameters. For this outdoor module temperature model, several simplifying scenarios can be considered (Table 4.1). Each scenario disables specific terms in the model equations Equation 3.14 and Equation 3.15. Assuming the proper combinations of those scenarios reduces the equations' complexity and reveals simpler connections between the processes. If this connection then contains a parameter of interest and it is possible to realise these conditions experimentally well enough, the gathered data can be used for parameter determination.

This calibration method has a couple of downsides. Firstly, it is not necessarily possible to determine all parameters in this way. Several parameters might need to be estimated - e.g. based on well-known physical literature values - because other parameters depend on them. These interdependencies can also force a specific order in which the parameters need to be determined. Secondly, through condensing the equations only characteristic parts of the model are examined at once. As a consequence, the model is never evaluated as a whole which may lead to inconsistencies. Section 4.2 introduces an approach of calibration that improves upon these particular difficulties. Nonetheless, calibration via construing the model equations yields solid basic parameter estimates. In the following sections, all parameters are determined sequentially using the classical approach of reorganising the model equations.

#### Dimensions $d_m$ and $h_m$

The outdoor module's dimensions can be determined by callipering:

$$d_m = 45 \text{ mm}, h_m = 105.3 \text{ mm} \quad (4.1)$$

Hence the exposed area is  $A_s = 164.77 \text{ cm}^2$  and the short-wave radiation receiving area is  $A_r = 47.39 \text{ cm}^2$ .

**Table 4.1:** Simplifying experimental scenarios

Scenario	Condition	Explanation
dry	$a_{\text{wet}} = 0$	surface completely dry
wet	$a_{\text{wet}} = 1$	surface as wet as possible, e.g. thin wet fabric cover
dark	$I_{\text{sw}} = 0$	no short-wave radiation, e.g. dark room
calm	$v = 0$	no wind, e.g. indoors
ventilated	$v > 0$	windy
stationary	$\frac{dT_s}{dt} = \frac{dT_i}{dt} = 0$ and $T_s = T_i$	the system's physical state is constant in time

### Surface Short-Wave Albedo $\alpha_s$

Determining the short-wave albedo of a flat extensive horizontal area is possible by relating the incoming and reflected short-wave radiation, e.g. with pyranometer measurements (Payne 1972, sea surface albedo). Unfortunately, the outdoor module's short-wave radiation receiving surface is neither flat, nor horizontal, nor large. Instead it is cylindrical and with less than  $1 \text{ dm}^2$  of area also rather small. For this reason, as pyranometers can only be used reliably for hemispherical measurements, they are an inappropriate choice in this case. The common methods for determining the albedo of a surface thus cannot be applied to the outdoor module and an alternative technique has to be used.

Standard digital cameras' CCD sensors are basically arrays of light-sensitive electrical components. Therefore they can also be used to estimate short-wave radiation, either over the whole image or even single spots (Rossini and Krenzingler 2007; Chauvin et al. 2015; Kurtz and Kleissl 2017). This can be used to overcome the mentioned spot-measuring limitations of pyranometers: with a digital camera, the brightness (i.e. the reflected irradiance) of a specific point can be proxied qualitatively using the monochrome pixel luminance value (ITU Radiocommunication Assembly 1995; Watson et al. 2001). To estimate the cover albedo  $\alpha_s$ , the method introduced by Gilchrist (2011) is extended slightly. The outdoor module is placed alongside two materials that have well-known 'extreme' albedos and a picture is taken, preferably with a bright light (e.g. sunlight) shining from behind. The brightnesses of the known materials can then be used to interpolate the cover's surface albedo  $\alpha_s$  over its own luminance value.

The two albedo references used here are a hole to a black hollow body ( $\alpha \approx 0$ ) and white office paper ( $\alpha \approx 0.65$ , Gilchrist 2011) as shown in Figure 4.1. The experiment was conducted indoors with moderate incoming sunlight. For the cover surface, this experiment yielded an albedo of  $\alpha_s \approx 0.50$ . Undeniably, the outdoor module's cylindrical shape raises issues with this method because the incoming light is reflected into different directions as clearly visible in the image. To address this, only the brightest region of the cover surface was taken into account for the albedo interpolation because this is the region where the effective incoming light beam hits the surface.

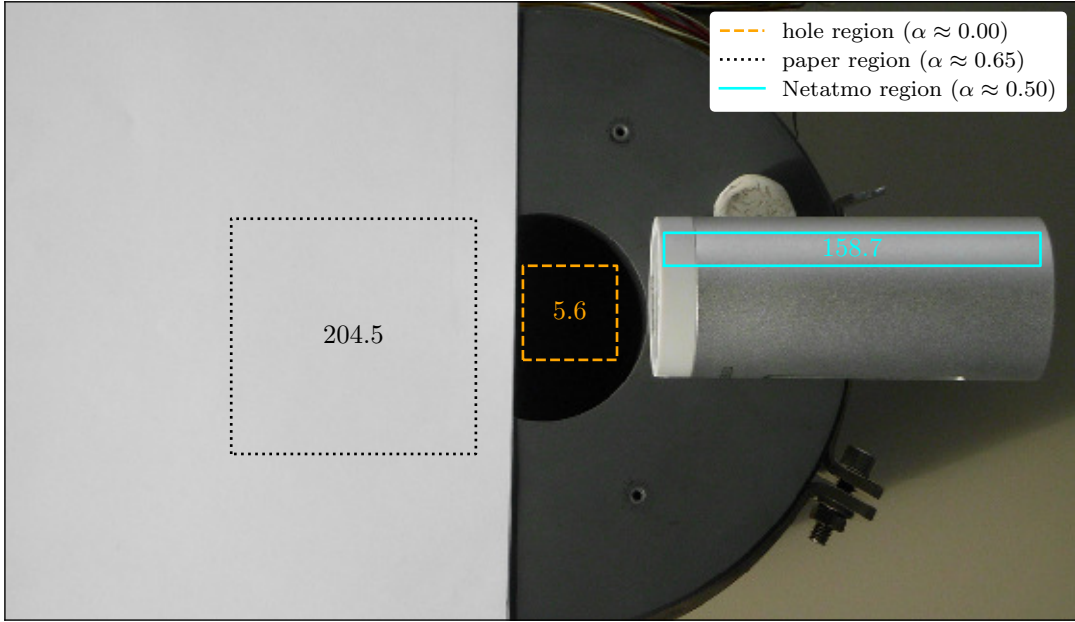


**Figure 4.1:** Albedo determination experiment. The outdoor module was placed alongside office paper (albedo  $\alpha \approx 0.65$ ) and a hole to a black hollow body (albedo  $\alpha \approx 0.0$ ). The numbers indicate the mean luminance value ( $0 \leq L \leq 255$ ) in the box region used to interpolate the cover's albedo ( $\alpha_s \approx 0.50$ ).

### Surface Long-Wave Emissivity $\varepsilon_s$

The emissivity  $\varepsilon$  of a surface is defined as the ratio of its emitted radiation intensity to the corresponding blackbody radiation (cf. text books like Wallace and Hobbs 2006). The intrinsic dependency on wavelength is neglected here for simplicity.

Using a device measuring radiation temperature  $T_{\text{rad}}$  with a fixed emissivity setting (in use for this experiment: HEITRONICS KT19 radiation pyrometer (KT19),  $\varepsilon_{\text{rad}} = 1$ ), the cover surface's emissivity can be determined based on a radiation intensity balance. The device receives radiation of two sources, on the one hand the emitted radiation from the cover itself and on the other hand the reflected radiation originating from the surrounding room walls and furniture. Assuming that the room temperature  $T_r$  is equal to the air temperature  $T_a$  and the interior walls all have a homogeneous emissivity, the total incoming long-wave radiation can be parametrised as the room's blackbody radiation because all of the reflected room radiation accumulates eventually:

$$I_{\text{lw}_{\text{in}}} = \sigma T_r^4 = \sigma T_a^4 \quad (4.2)$$

The balance can then be formulated according to the STEFAN-BOLTZMANN-law:

$$\varepsilon_{\text{rad}} \sigma T_{\text{rad}}^4 = \varepsilon_s \sigma T_s^4 + (1 - \varepsilon_s) \sigma T_a^4 \quad (4.3)$$

Rearranging yields the relationship to determine the cover's emissivity  $\varepsilon_s$ :

$$\varepsilon_s = \frac{\varepsilon_{\text{rad}} T_{\text{rad}}^4 - T_a^4}{T_s^4 - T_a^4} \quad (4.4)$$

The maximum error in the emissivity can then be estimated based on the input quantities' maximum errors  $\Delta T_{\text{radmax}}$ ,  $\Delta T_{\text{smax}}$  and  $\Delta T_{\text{amax}}$  assuming that  $T_a < T_{\text{rad}} < T_s$ :

$$\begin{aligned} \Delta \varepsilon_{\text{smax}} &= \left| \frac{\partial \varepsilon_s}{\partial T_{\text{rad}}} \right|_{\overline{T_{\text{rad}}}} \Delta T_{\text{radmax}} + \left| \frac{\partial \varepsilon_s}{\partial T_s} \right|_{\overline{T_s}} \Delta T_{\text{smax}} + \left| \frac{\partial \varepsilon_s}{\partial T_a} \right|_{\overline{T_a}} \Delta T_{\text{amax}} \\ &= \frac{4}{\overline{T_s}^4 - \overline{T_a}^4} \left[ \Delta T_{\text{radmax}} \varepsilon_{\text{rad}} \overline{T_{\text{rad}}}^{-3} + \Delta T_{\text{smax}} \overline{\varepsilon_s} \overline{T_s}^{-3} + \Delta T_{\text{amax}} (1 - \overline{\varepsilon_s}) \overline{T_a}^{-3} \right], \end{aligned} \quad (4.5)$$

where  $\overline{\varepsilon_s}$  denotes the emissivity according to Equation 4.4 but calculated with average values. The denominator in Equation 4.4 implies that this formula can only be applied if there is a significant difference in cover surface temperature  $T_s$  and air temperature  $T_a$ . Furthermore Equation 4.5 shows that the error is decreased in this case. Hence, all outdoor modules are heated up in the climate chamber until a stationary temperature reading  $T_m$  is achieved. Taken out of the climate chamber, the outdoor modules are then immediately arranged in a wall-like setup to make sure that the KT19 receives the full radiation intensity (Figure 4.2a). The effective temperature of this cover-wall can then be estimated by their mean readings:  $T_s = \overline{T_m}$ , while the indoor modules residing in the same room provide air temperature  $T_a$ .

Having heated up the outdoor modules to around  $T_m \approx 46^\circ\text{C}$ , an emissivity of  $\overline{\varepsilon_s} \approx 0.778$  is obtained. To estimate the error of this result, the uncertainties are assumed to have magnitudes of  $\Delta T_{\text{radmax}} = 2\text{ K}$ ,  $\Delta T_{\text{smax}} = 0.50\text{ K}$  and  $\Delta T_{\text{amax}} = 2\text{ K}$ . This yields a maximum relative error of  $\frac{\Delta \varepsilon_{\text{smax}}}{\overline{\varepsilon_s}} \approx 13\%$ .

## Internal Conductivity $\lambda$

Unfortunately, there is no trivial way of determining the internal conductivity  $\lambda$  without knowing several other parameters because no scenario (Table 4.1) connects it solely to the already-determined ones ( $h_m$ ,  $d_m$ ,  $\varepsilon_s$  and  $\alpha_s$ ). Hence, the effective internal conductivity has to be estimated. This can be done by calculating a weighted sum of the different materials' conductivities present in the module, i.e. air ( $\approx 0.025\text{ W m}^{-1}\text{ K}^{-1}$ , Weast 1981) and plastic ( $\approx 0.25\text{ W m}^{-1}\text{ K}^{-1}$ , Speight et al. 2005). As mentioned before, the cover has direct contact to the sensor unit on its fastening ring. So the sensor unit plastic's conductivity presumably has greater share in the internal conductivity than the air's. Thus, the internal conductivity is arbitrarily chosen to be  $\lambda = 0.2\text{ W m}^{-1}\text{ K}^{-1}$ .

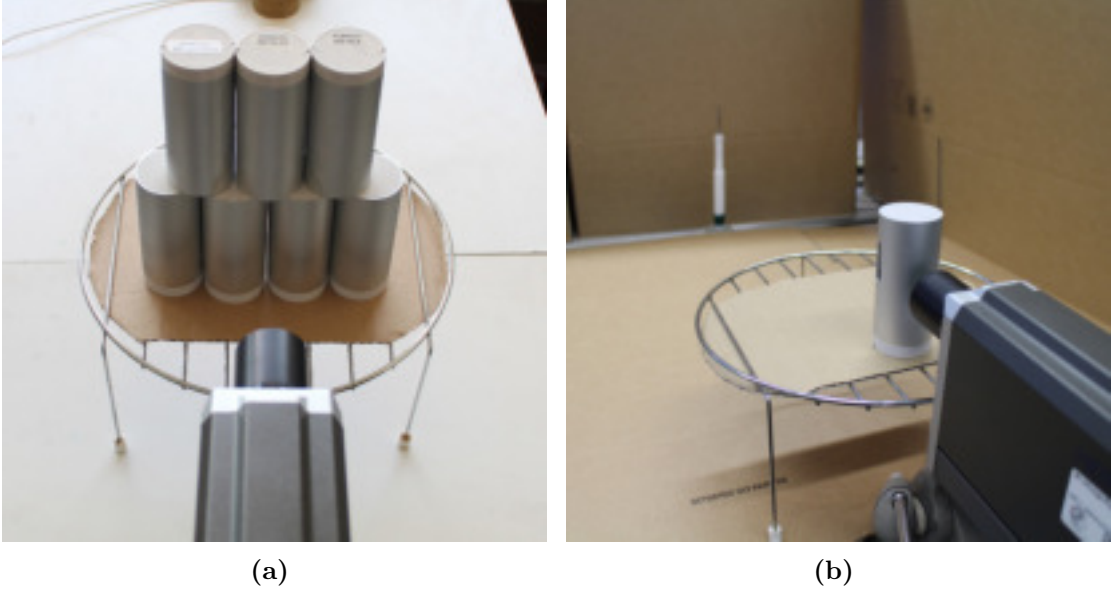


**Figure 4.2:** Emissivity (a) and effective cover and sensor unit heat capacity determination experiment setup (b). In both experiments the Netatmo outdoor modules were heated up in the climate chamber and the cover surface’s radiation temperature was measured with a KT19. The room temperature was measured with a HMP (white vertical staff in the background).

### Effective Cover Heat Capacity $C_s$

To determine the effective cover heat capacity, a dry, dark and calm scenario is useful. Equation 3.14 then reduces to

$$\underbrace{\frac{C_s}{A_s} \frac{dT_s}{dt}}_{\text{cover thermal inertia}} = \underbrace{-\varepsilon_s \sigma T_s^4}_{\text{long-wave out}} + \underbrace{+\varepsilon_s I_{\text{lw in}}}_{\text{long-wave in}} - \underbrace{\frac{\lambda}{d_m} (T_s - T_i)}_{\text{internal heat conduction}} . \quad (4.6)$$

The total incoming long-wave radiation  $I_{\text{lw in}}$  can be again parametrised by means of air temperature (Equation 4.2), simplifying Equation 4.6 to

$$\underbrace{\frac{C_s}{A_s} \frac{dT_s}{dt}}_{\text{cover thermal inertia}} = \underbrace{\varepsilon_s \sigma (T_a^4 - T_s^4)}_{\text{radiation budget}} - \underbrace{\frac{\lambda}{d_m} (T_s - T_i)}_{\text{internal heat conduction}} . \quad (4.7)$$

This leaves only the long-wave radiation budget, the cover’s thermal inertia and the internal heat conduction, all of which are quantifiable as the needed parameters are determined by now. To determine the effective cover heat capacity  $C_s$ , all outdoor modules were heated up in the climate chamber. When the reading became stationary, each outdoor module was placed on a desk to measure the decay in surface radiation temperature  $T_{\text{rad}}$  (KT19), along with the module temperature  $T_m = T_i$  (Equation 3.3) and the surrounding air temperature  $T_a$  (HMP) as seen in Figure 4.2b. To convert the measured surface radiation temperature  $T_{\text{rad}}$  to the surface

temperature  $T_s$ , Equation 4.3 can be rearranged:

$$T_s = \sqrt[4]{\frac{\varepsilon_{\text{rad}} T_{\text{rad}}^4 - (1 - \varepsilon_s) T_a^4}{\varepsilon_s}} \quad (4.8)$$

Discretizing the surface temperature tendency  $\frac{dT_s}{dt}$  enables the determination of the cover heat capacity  $C_s$  by an offset-less linear regression of the surface energy budget over the surface temperature tendency:

$$C_s \underbrace{\frac{\Delta T_s}{\Delta t}}_{\text{cover temperature tendency}} = A_s \underbrace{\left[ \varepsilon_s \sigma (T_a^4 - T_s^4) - \frac{\lambda}{d_m} (T_s - T_i) \right]}_{\text{surface energy budget}} \quad (4.9)$$

The gain of this fit is then equal to the effective cover heat capacity. As the KT19 has a high temporal resolution ( $\Delta t = 1$  s, as opposed to the minutely outdoor module data), the readings were smoothed with a moving 120 s-window to reduce the noise in the KT19 temperature reading. The regression results can be seen in Figure 4.3.

Pure aluminium has a specific heat capacity of around  $900 \text{ J K}^{-1} \text{ kg}^{-1}$  (Weast 1981). Thus, if the cover consisted of aluminium only, its actual heat capacity would be  $73.62 \text{ J K}^{-1}$ , taking its whole weight into account (Table 2.1). This is well in line with the mean experimental result of  $C_s \approx 49.33 \text{ J K}^{-1} \pm 3\%$ . The effective cover heat capacity is lower because - deviating from simplification Table 3.1I - the temperature sensor is in fact quite near to one cover spot (Figure 2.2). Therefore, the actual cover mass directly involved in the heat exchange with the sensor unit is lower than the whole cover's mass.

### Effective Sensor Unit Heat Capacity $C_m$

Analogously to the effective cover heat capacity, the effective sensor unit heat capacity  $C_m$  can be estimated based on the same experiment, but discretizing the sensor unit energy balance Equation 3.15 instead:

$$C_m \underbrace{\frac{\Delta T_i}{\Delta t}}_{\text{sensor unit temperature tendency}} = \lambda \underbrace{\frac{A_s}{d_m} (T_s - T_i)}_{\text{internal heat transfer}} \quad (4.10)$$

Again, the gain of an offset-less linear regression of the internal heat transfer over the sensor unit temperature tendency can then be used as an estimate of the effective sensor unit heat capacity  $C_m$  (Figure 4.4). For this analysis the readings were smoothed with a 300 s-window to reduce the KT19 noise even further. It turns out that the regression for the sensor unit heat capacity has a significantly larger relative uncertainty ( $C_m = 24.49 \text{ J K}^{-1} \pm 18\%$ ). This is a consequence of the internal heat transfer being one order of magnitude smaller than the surface energy budget. Therefore, Equation 4.10 is more prone to measurement uncertainties than Equation 4.9. Nonetheless it is realistic that the effective sensor unit heat capacity is smaller than the cover heat capacity ( $C_m < C_s$ ) due to the component's different masses.

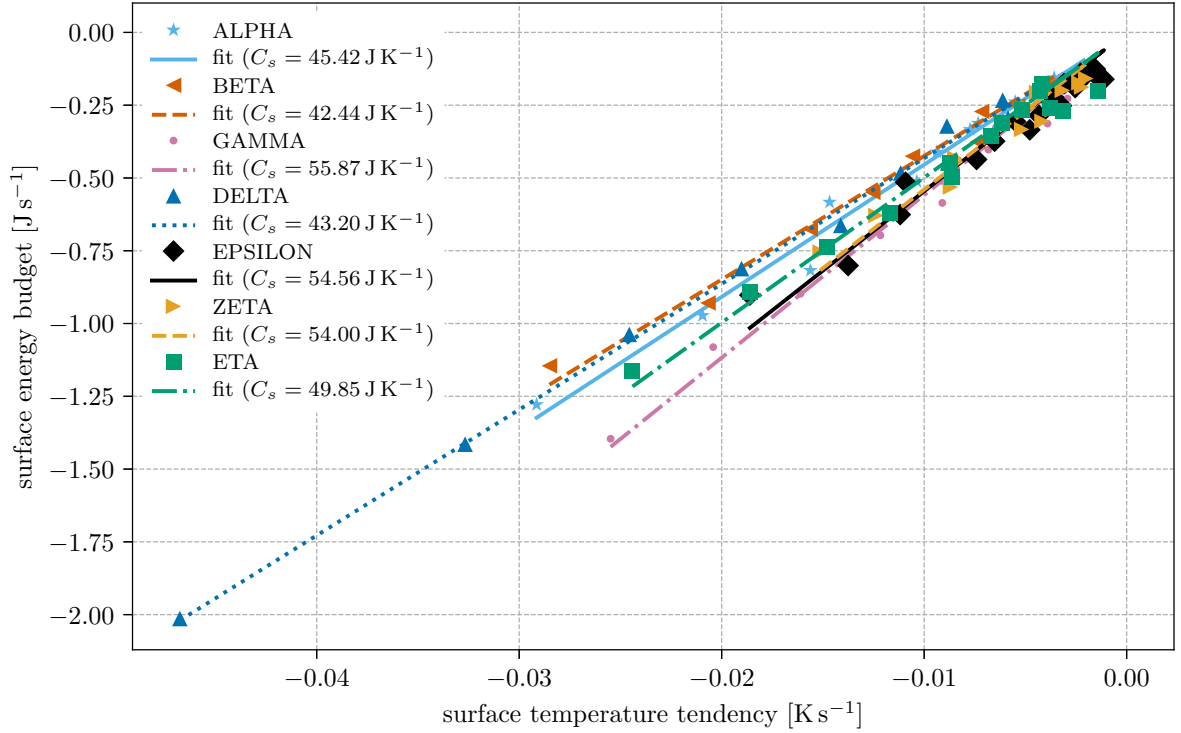


**Figure 4.3:** Offset-less linear regression of the surface energy budget over the cover surface temperature tendency. The gain is an estimate of the effective cover heat capacity  $C_s \approx 49.33 \pm 3\%$ .

### Bulk Transfer Coefficient $\eta$

The bulk transfer coefficient  $\eta$  can be determined when allowing for a ventilated scenario. Along with dry and dark conditions, Equation 3.14 reduces to:

$$\underbrace{\frac{C_s}{A_s} \frac{dT_s}{dt}}_{\text{cover thermal inertia}} = \underbrace{-\varepsilon_s \sigma T_s^4}_{\text{long-wave out}} + \underbrace{+\varepsilon_s I_{lw\text{in}}}_{\text{long-wave in}} - \underbrace{\rho_a c_p (T_s - T_a) \eta v}_{\text{sensible heat flux}} - \underbrace{\frac{\lambda}{d_m} (T_s - T_i)}_{\text{internal heat conduction}} \quad (4.11)$$

Once more, the total incoming long-wave radiation is parametrised in terms of room temperature  $T_r$  (Equation 4.2). This simplifies Equation 4.11 to

$$\underbrace{\frac{C_s}{A_s} \frac{dT_s}{dt}}_{\text{cover thermal inertia}} - \underbrace{-\varepsilon_s \sigma (T_r^4 - T_s^4)}_{\text{radiation budget}} + \underbrace{\frac{\lambda}{d_m} (T_s - T_i)}_{\text{internal heat conduction}} = \underbrace{-\rho_a c_p (T_s - T_a) \eta v}_{\text{sensible heat flux}} \quad (4.12)$$

which relates the cover's energy budget (left-hand side) to the sensible heat flux (right-hand side) containing the parameter  $\eta$  of interest. To quantify this relationship, an experimental setup is required that allows for exposing the outdoor module to wind of different temperatures ( $T_a$ ) and velocities ( $v$ ) while also observing its exact surface temperature  $T_s$ . In this

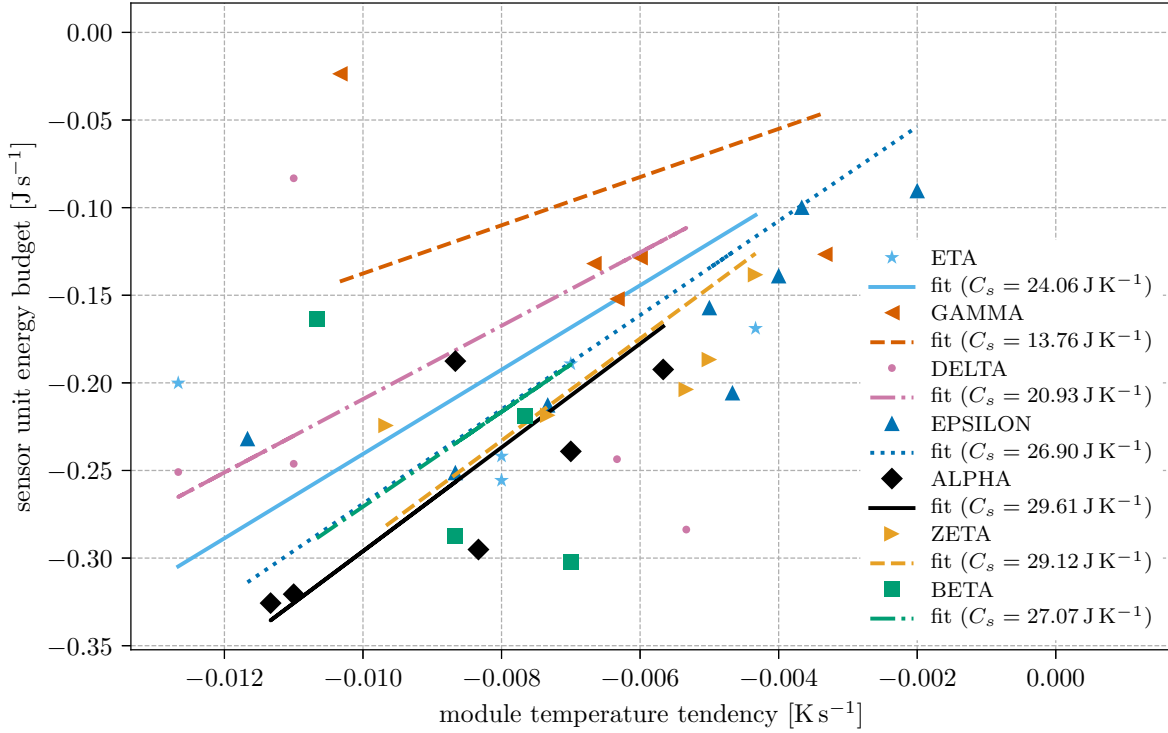


**Figure 4.4:** Offset-less linear regression of the internal heat transfer over the sensor unit temperature tendency. The gain is an estimate of the effective sensor unit heat capacity  $C_m \approx 24.49 \text{ J K}^{-1} \pm 18 \%$ .

experimental setting, three standard hair-dryers were used to create the wind (Figure 4.5). Switching one or more hair-dryers at varying intensities easily makes a range of different wind velocity/air temperature combinations possible. Wind velocity  $v$  was measured with a KAINDL ELECTRONIC Windmaster 2, cover surface temperature  $T_s$  with the KT19 and the wind's air temperature  $T_a$  with the HMP (Figure 4.5b). For the room temperature  $T_r$ , the indoor modules' temperature measurement was used. The dry air density  $\rho_a$  can be derived from the indoor modules' pressure reading  $p$  and the air temperature in immediate proximity of the cover  $T_a$  applying the ideal gas law:

$$\rho_a = \frac{p}{R_d T_a}, \quad (4.13)$$

with  $R_d = 287 \text{ J kg}^{-1} \text{ K}^{-1}$  (Wallace and Hobbs 2006) denoting the specific gas constant of dry air. To align the measurements and remove noise the readings were smoothed with a moving 120 s-window.

Theoretically, the bulk transfer coefficient  $\eta$  should then be determinable analogously to the heat capacities by an offset-less linear regression of the cover's energy budget over the parameter-less part of the sensible heat flux. However, Figure 4.6 reveals that for higher-temperature winds (devices BETA and ZETA) the cover's energy budget (the left-hand side of Equation 4.12) is obviously unclosed as the slope of the data still suggests an energy excess even when the sen-

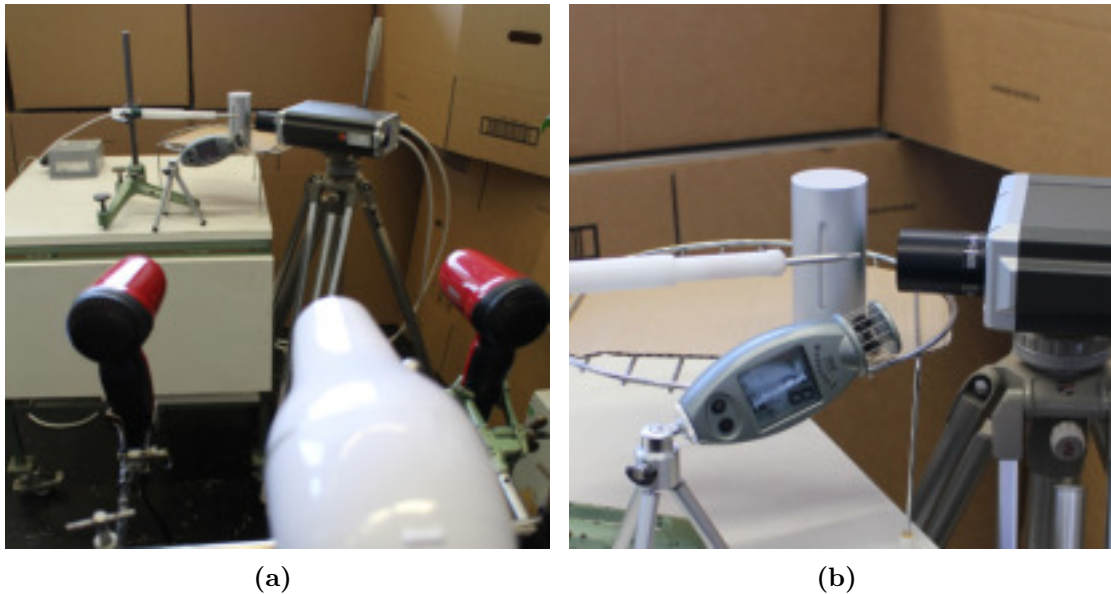


**Figure 4.5:** Setup of the bulk transfer coefficient experiment. (a) Three hair-dryers were used to simulate wind of different temperatures and velocities. (b) Detailed view - white staff: HMP, right-hand side: KT19, bottom: Windmaster, center: outdoor module

sible heat flux vanishes. So evidently the sensible heat flux parametrisation (Equation 3.9) is lacking another additive term that is proportional to the air temperature  $T_a$  and independent of the wind velocity  $v$ . This is a consequence of neglecting sensible and latent heat fluxes under calm conditions (Table 3.1VIII). Nonetheless, the gain of the regression still gives an estimate of the wind-induced bulk transfer coefficient consistent with the used parametrisation:  $\eta \approx 0.0134 \pm 15\%$ . This coincides with common values for the bulk transfer coefficient of the earth's surface (0.001 to 0.005 under neutral conditions, but up to three times as large under turbulence, Wallace and Hobbs 2006).

The final parameter values resulting from condensing the equations are listed in Table 4.2.

## 4.2 Optimization

All of the previous calibration steps only include specific parts of the model equations. As seen above in the calibration of the bulk transfer parameter  $\eta$ , this can lead to overall inconsistencies. For fine-tuning the calibration results while incorporating the whole model instead of just particular portions of it, an optimization will be performed. The general aim of an optimization is to determine the input of a system needed to obtain a specific desired outcome. A wide range of numerical optimization techniques is available (see e.g. Nocedal and Wright 2000) essentially designed to minimize an arbitrary function. If this function is configured as the difference between a system's output and the desired output, the optimization effectively yields the corresponding system's input. Especially if the system is heavily non-linear an optimization can be a viable method of inversion (Chapter 7).

Applied to fine-tuning the model calibration, the optimization concept is depicted schematically in Figure 4.7. Having initially estimated the parameters and using the forcing of a previously con-

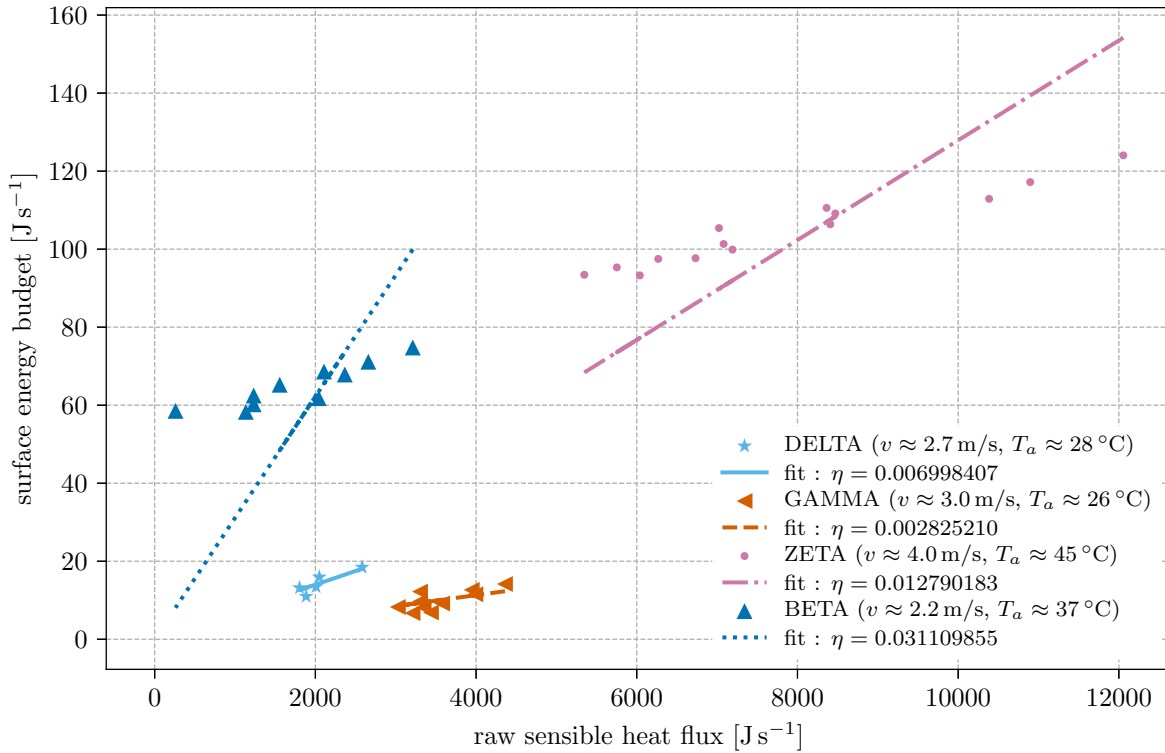


**Figure 4.6:** Offset-less linear regression of the raw sensible heat flux over the surface energy budget. The gain is an estimate of the bulk transfer coefficient  $\eta \approx 0.0134 \pm 15\%$ .

ducted experiment, the outdoor module temperatures  $T_s$  and  $T_i$  are simulated with the model. The results are then compared to the real temperature measurements. According to the optimization algorithm another estimate for the parameters is then assumed to repeat the procedure until the simulated temperatures match the measured temperatures best. In this study, the SciPy (Jones et al. 2001) implementation of the L-BFGS-B bound-constrained optimization algorithm introduced by Byrd et al. (1995) and Zhu et al. (1997) was used because of its robustness and handling of bounded input.

As in the bulk transfer coefficient experiment enough necessary data is available for precise re-simulation, the outdoor module's readings from that experiment are now used as the reference state and the forcing during that experiment is adopted for the upcoming simulation. As a first parameter guess, the previously determined values are taken from Table 4.2. To assess the resemblance of modelled and reference state, the average root mean squared error (RMSE) of both simulated and measured temperature time series in  $T_s$  and  $T_i$  respectively is used. The albedo  $\alpha_s$  and the emissivity  $\varepsilon_s$  are left unchanged as the measurements didn't provide data accurate enough for their quantification. Furthermore, an upper constraint of  $\eta \leq 0.1$  was defined for stability reasons.

In the bulk transfer coefficient experiment (Figure 4.6) the devices GAMMA and DELTA were best in line with the model equations. This also shows in the optimization results (Figure 4.8). In contrast to the simulation with the unoptimized parameters, the RMSE between simulated and measured temperature time series has decreased substantially through the optimization.

**Table 4.2:** Calibration results by construing the equations

Parameter	Value	Uncertainty
$h_m$	105.3 mm	–
$d_m$	45 mm	–
$\alpha_s$	0.50	–
$\varepsilon_s$	0.78	$\pm 13\%$
$\lambda$	$0.200 \text{ W m}^{-1} \text{ K}^{-1}$	–
$C_s$	$49.33 \text{ J K}^{-1}$	$\pm 3\%$
$C_m$	$24.49 \text{ J K}^{-1}$	$\pm 18\%$
$\eta$	0.0134	$\pm 15\%$

However, the optimization for the devices BETA and ZETA (Figure 4.9), whose readings had a significantly unclosed energy budget, is reaching its limit in credibility. The RMSE is still significantly decreased and while especially the sensor unit temperature simulation matches its reading counterpart very well, the simulated cover temperature is still strikingly off. The optimization cannot balance the insufficient parametrisation. This is also expressed by the optimized bulk transfer parameter being exactly at the upper constraint value of  $\eta = 0.1$ . Thus, the optimization for these devices is ignored.

Nevertheless, for the devices GAMMA and DELTA the optimization suggests a decreased bulk transfer coefficient and a decreased internal conductivity. Therefore, they are further set to the mean optimized values of  $\eta \approx 0.0051$  and  $\lambda \approx 0.082 \text{ W K}^{-1} \text{ m}^{-1}$ . The optimization left the heat capacities practically untouched which indicates that variations in the heat capacities have smaller effects on the simulated temperature as the internal conductivity and the bulk transfer parameter for this experiment. The final parameters after the optimization are listed in Table 4.3.

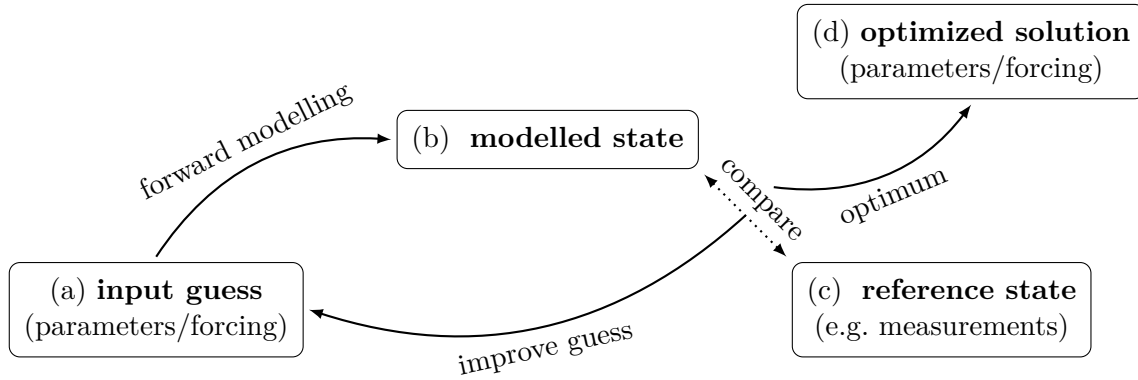
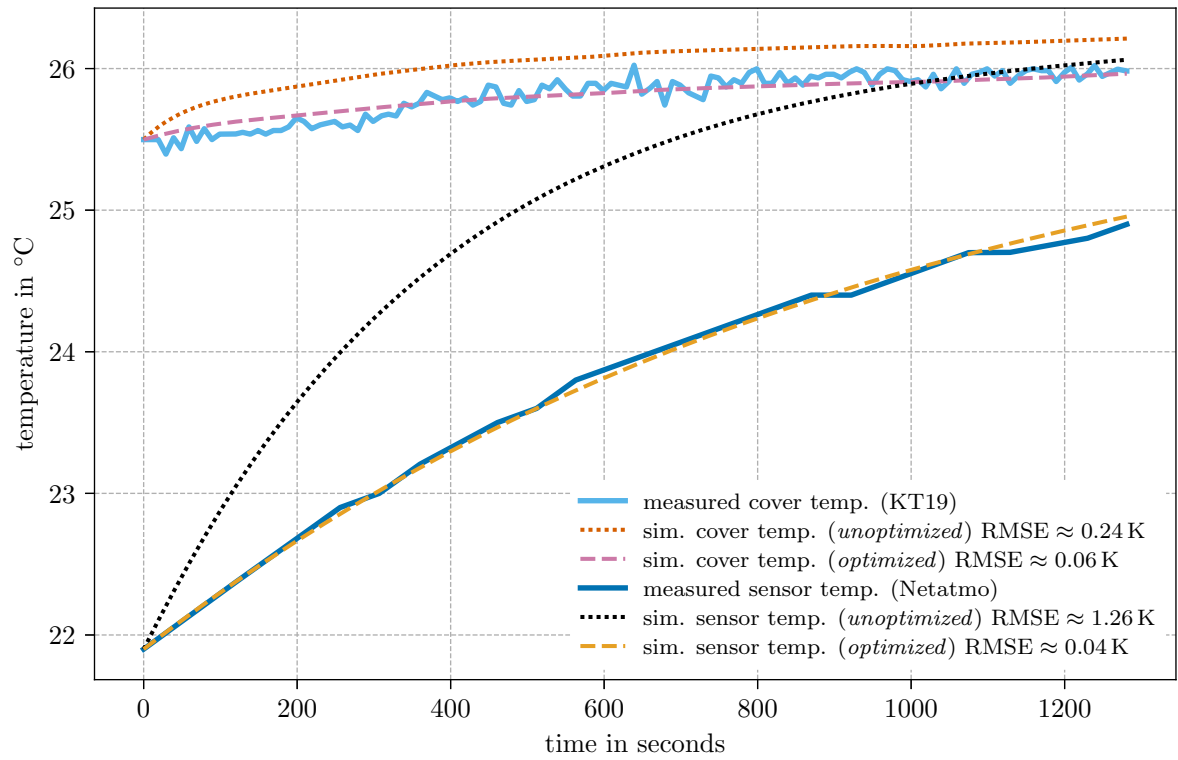


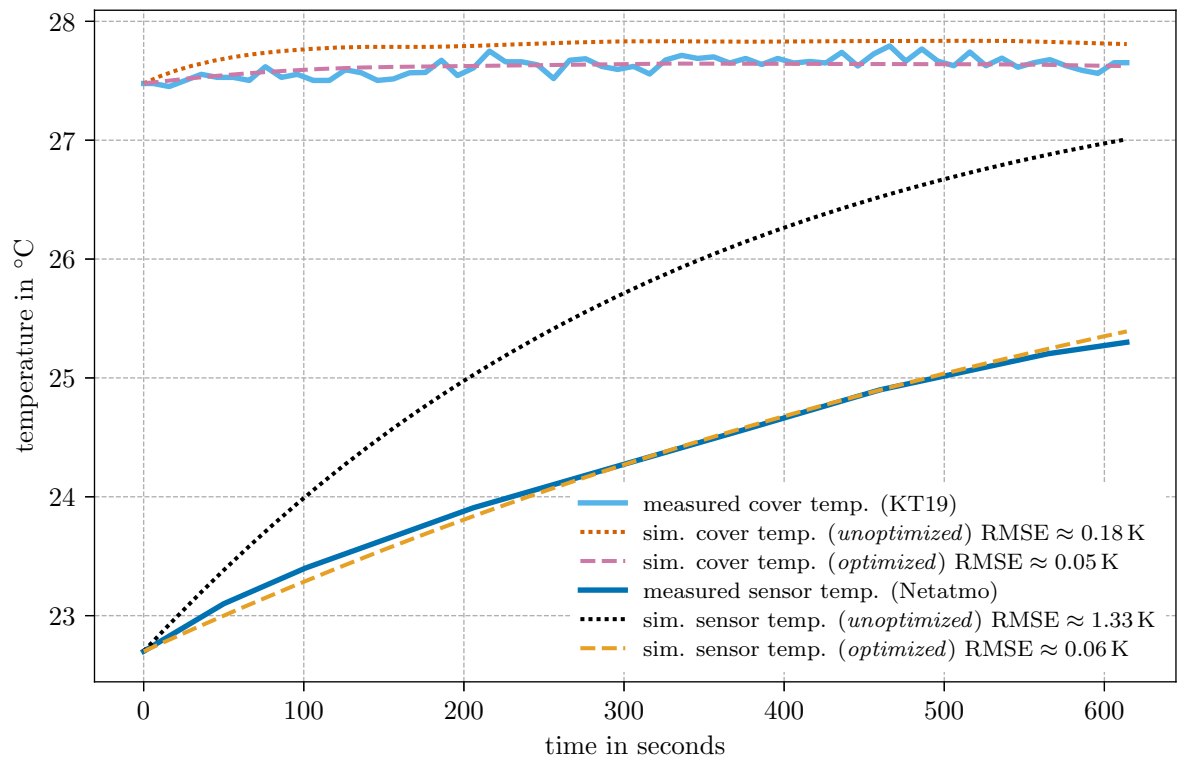
**Figure 4.7:** The concept of model optimization. All parameters and forcing of interest are guessed (a) to determine the model output (b). Depending on a comparison of the modelled and a reference state (c) the guess is improved and the process repeated until an optimum (d) is reached.

**Table 4.3:** Calibration results after optimization

Parameter	Value
$h_m$	105.3 mm
$d_m$	45 mm
$\alpha_s$	0.50
$\varepsilon_s$	0.78
$\lambda$	$0.082 \text{ W m}^{-1} \text{ K}^{-1}$
$C_s$	$49.33 \text{ J K}^{-1}$
$C_m$	$24.53 \text{ J K}^{-1}$
$\eta$	0.0051

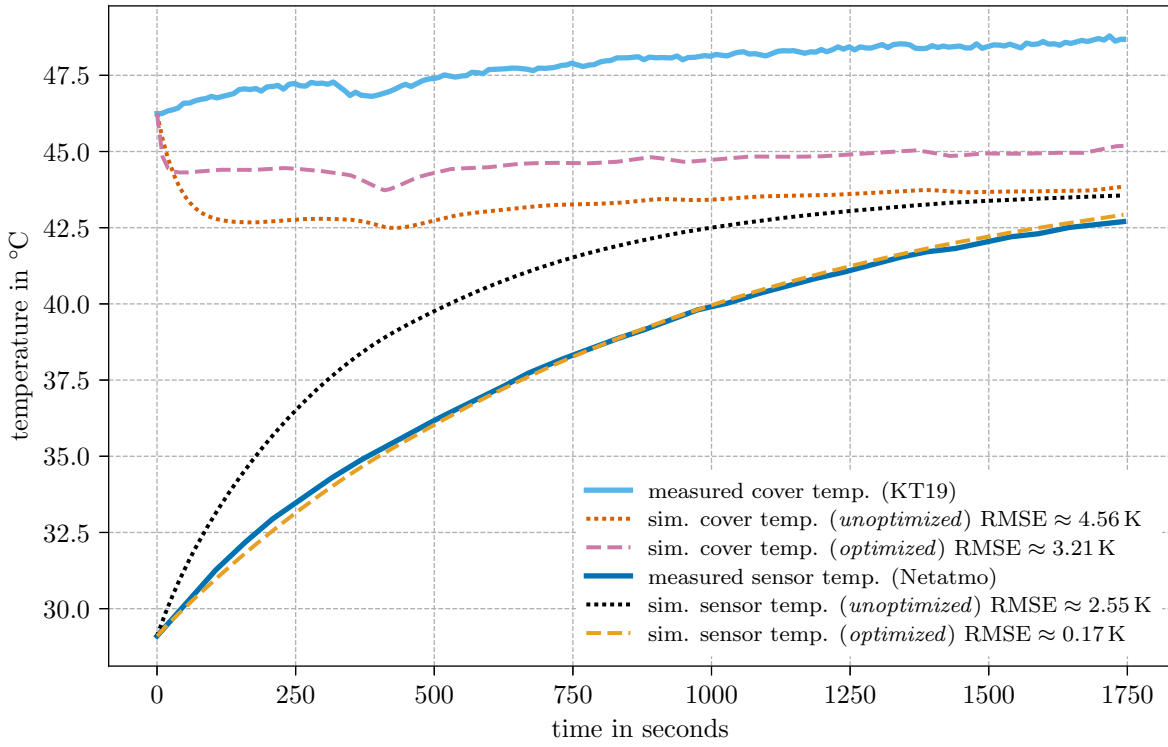


(a)

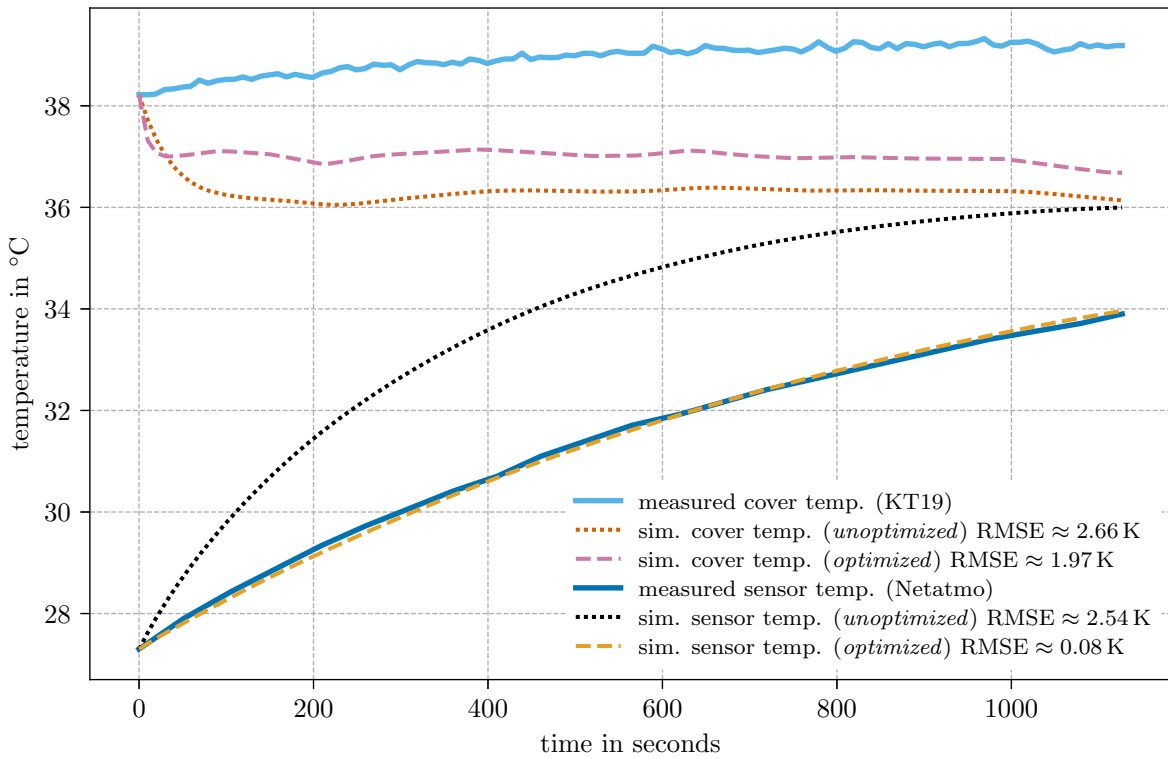


(b)

**Figure 4.8:** Optimization results of the bulk transfer parameter experiment data,  
 (a) Device GAMMA:  $C_s \approx 49.33 \text{ J K}^{-1}$ ,  $C_m \approx 24.52 \text{ J K}^{-1}$ ,  $\lambda \approx 0.077 \text{ W m}^{-1} \text{ K}^{-1}$ ,  $\eta \approx 0.0056$ ,  
 (b) Device DELTA:  $C_s \approx 49.33 \text{ J K}^{-1}$ ,  $C_m \approx 24.53 \text{ J K}^{-1}$ ,  $\lambda \approx 0.086 \text{ W m}^{-1} \text{ K}^{-1}$ ,  $\eta \approx 0.0047$



(a)



(b)

**Figure 4.9:** Optimization results of the bulk transfer parameter experiment data,  
 (a) Device ZETA:  $C_s \approx 49.33 \text{ J K}^{-1}$ ,  $C_m \approx 24.58 \text{ J K}^{-1}$ ,  $\lambda \approx 0.082 \text{ W m}^{-1} \text{ K}^{-1}$ ,  $\eta \approx 0.1000$ ,  
 (b) Device BETA:  $C_s \approx 49.33 \text{ J K}^{-1}$ ,  $C_m \approx 24.56 \text{ J K}^{-1}$ ,  $\lambda \approx 0.069 \text{ W m}^{-1} \text{ K}^{-1}$ ,  $\eta \approx 0.1000$

# Chapter 5

## Implications

With the calibrated parameters determined in Chapter 4, it is possible to simulate the measurement of a Netatmo outdoor module under given environmental conditions. In the following, the readings of a Netatmo outdoor module are simulated at the Wettermast Hamburg measurement site and discussed with a focus on examining whether the Netatmo outdoor module really measures the surrounding air temperature. Furthermore, to investigate the influence of the outdoor module's construction on its measurement, scenarios modifying the outdoor module's material properties in the model are introduced and compared to the unmodified simulation.

### 5.1 Model Setup and Forcing

The Wettermast Hamburg measurement site (Brümmer et al. 2012) is a 280 m high broadcasting tower equipped with meteorological measurement devices in several heights. For the simulations, the readings in 2 m height above ground of the secondary mast were used as forcing for the model. This 12 m-high mast is located on a meadow in 170 m distance to the main tower. A two-year dataset ranging from 4<sup>th</sup> January, 2016 to 12<sup>th</sup> February, 2018 was used.

The site provides measurements of the forcing needed by the model as listed in Table 3.2c: global sky long-wave radiation  $I_{lw,sky}$ , global short-wave radiation  $I_{sw}$ , wind velocity  $v$ , air temperature  $T_a$ , ground surface temperature  $T_g$  (KT19), pressure  $p$  and relative humidity  $RH$ . The air density  $\rho_a$  and the specific humidity  $q_a$  were derived from the other values.

To parametrise the cover's wet area coverage  $a_{wet}$ , the infrared precipitation detection signal was used. If any precipitation was detected, the cover's wet area coverage was assumed to increase gradually over 10 minutes to the maximum amount of water it can hold. This maximum amount was set to 10 % based on empirical attempts to moisturise the outdoor module's surface. After the precipitation stopped, the cover's wet area coverage stays at its maximum for another 10 minutes, then decreases linearly to 0 % over 30 minutes.

The following simulations are intended to illustrate and examine what a Netatmo outdoor module would measure at the secondary Wettermast HH mast. As this site is very exposed, the simulation results cannot be transferred directly to real outdoor module measurements in urban areas. Nevertheless, the fundamental measurement characteristics can still be investigated.

### 5.2 Reference Simulation

The reference simulation was conducted with the original parameters listed in Table 4.3. The results for three exemplary weeks are shown alongside wind velocity and radiation input in Figure 5.1 (early spring), Figure 5.2 (summer) and Figure 5.3 (winter).

Several model properties are standing out. First, the influence of the short-wave radiation is clearly visible. During periods with high short-wave input (e.g. in summer, Figure 5.2) the

simulated outdoor module temperature is up to 5 K warmer than the forcing air temperature. This effect is increased at lower wind speeds (compare e.g. the last two days in Figure 5.1), which is well in line with the common perception of a temperature sensor that is exposed to direct sunlight.

Conversely, when the solar radiation vanishes in the night, the model predicts temperature drops of similar amplitude, especially under calm conditions as seen in Figure 5.2. As in calm and dry nights only the radiation budget remains, the simulated temperature drops below the air temperature. This drop is significantly dependent on the long-wave input as clearly noticeable in several nights in Figure 5.1 and Figure 5.2. Moreover, the dependency of the sensible heat flux on the wind velocity is distinctly observable in the night between the first two days in Figure 5.2. In this night the radiative forcing is constant but the wind velocity increases gradually. Although the air temperature diminishes, the simulated outdoor module temperature still increases due to the stronger influence of the sensible heat flux at higher wind speeds. However, part of this effect being so distinct is a consequence of neglecting the sensible heat flux under calm conditions (Table 3.1VIII) which effectively decouples the outdoor module from the surrounding air in situations with low wind speeds.

For the exemplary week in winter presented in Figure 5.3, the outdoor module temperature simulation is significantly better in line with the surrounding air temperature than for the other exemplary weeks. This is due to the lower amount of short-wave radiation and the generally smaller temperature variations during the winter season.

Altogether, this reference simulation exhibits an RMSE of 1.77 K between air temperature and simulated outdoor module temperature over the whole two-year time range (Figure 5.4a). A robust linear regression to minimize the effect of outliers (Huber 1964) reveals that the simulated outdoor module overestimates warmer air temperatures and underestimates colder air temperatures. Interestingly, the simulated outdoor module temperature follows the ground surface temperature closer than the air temperature. This is confirmed by a 33 % lower RMSE between simulated outdoor module temperature and ground surface temperature compared to air temperature (Figure 5.4). Furthermore, with an RMSE of under 1 K and an increased correlation of 99.5 %, the average of air and ground surface temperature is a better predictor for the simulated outdoor module temperature than either one of these quantities. The reverse conclusion of this finding is that instead of just air temperature, the temperature reading of an exposed outdoor module sited on a meadow is rather a proxy for a combination of air and ground surface temperature. Transferred to real Netatmo outdoor module measurements in urban areas this follows that outdoor module readings are more a representation of both air temperature and adjacent building blackbody temperature rather than just air temperature.

### 5.3 Influence of the Radiation Budget

To quantify the abovementioned strong influence of the radiation budget on the temperature measurement, simulations disabling parts of the radiation budget were conducted. Setting the albedo  $\alpha_s = 1$  effectively disables the solar input by assuming a perfectly blank surface, mirroring any short-wave radiation. Similarly, assuming an emissivity of  $\varepsilon_s = 0$  neglects both absorbed and emitted long-wave radiation which should roughly be the case for an extensively polished metal surface.

Assuming a full reflective cover without any radiation influence ( $\alpha_s = 1$  and  $\varepsilon_s = 0$ ), the

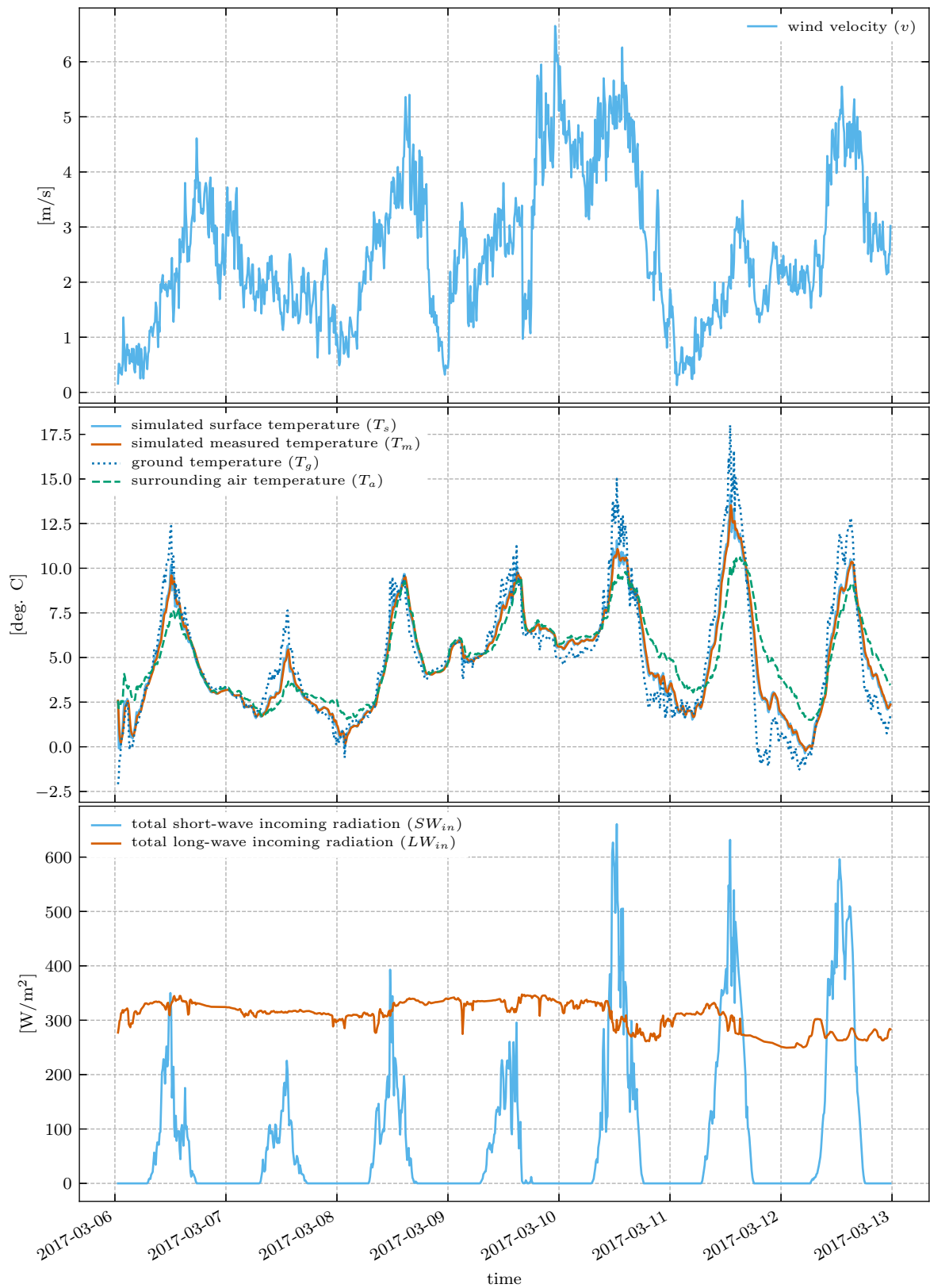


**Figure 5.1:** Simulated Netatmo outdoor module temperature alongside Wettermast HH forcing with original parameters (Table 4.3) during one spring week in 2017.

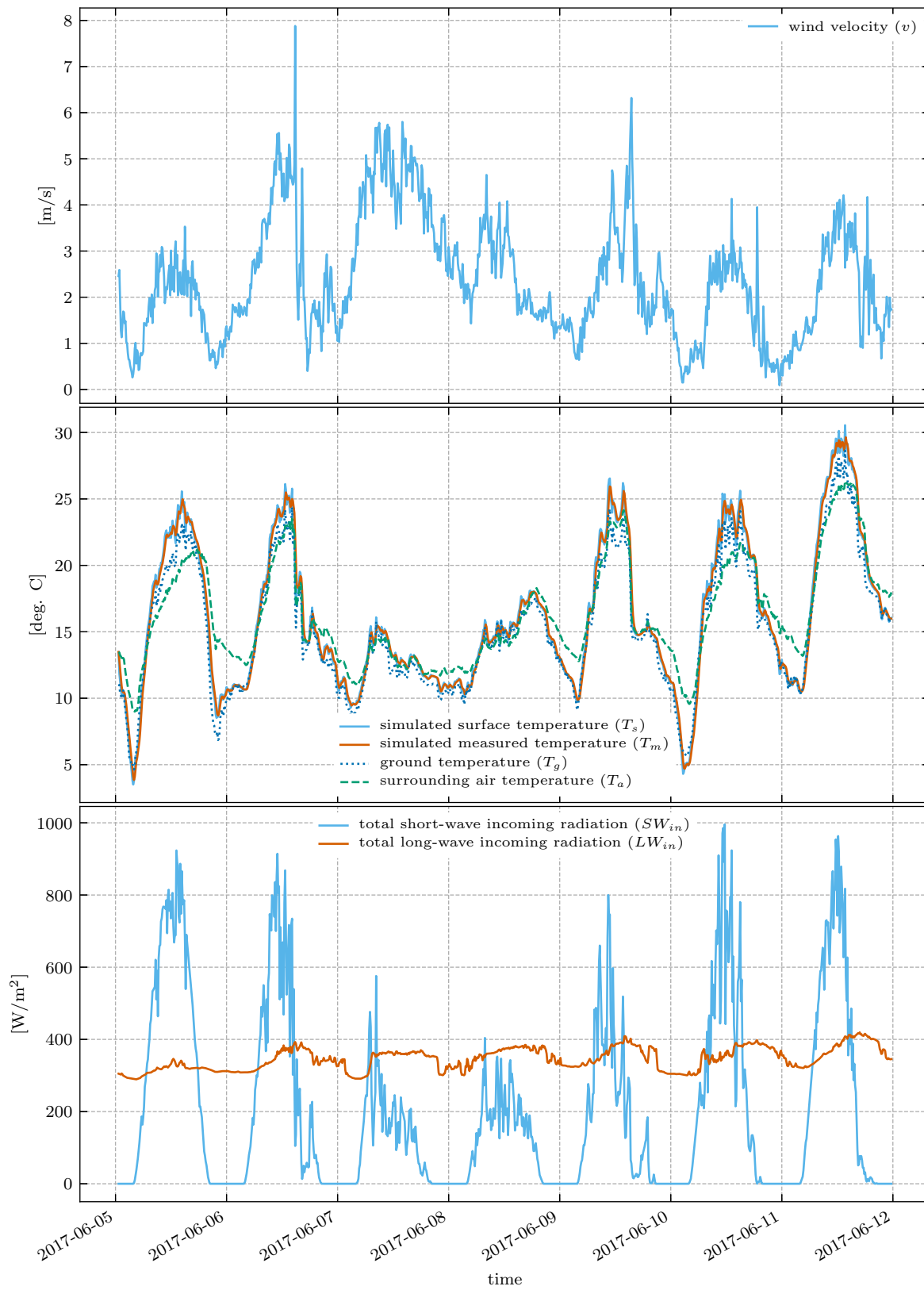


**Figure 5.2:** Simulated Netatmo outdoor module temperature alongside Wettermast HH forcing with original parameters (Table 4.3) during one summer week in 2017.

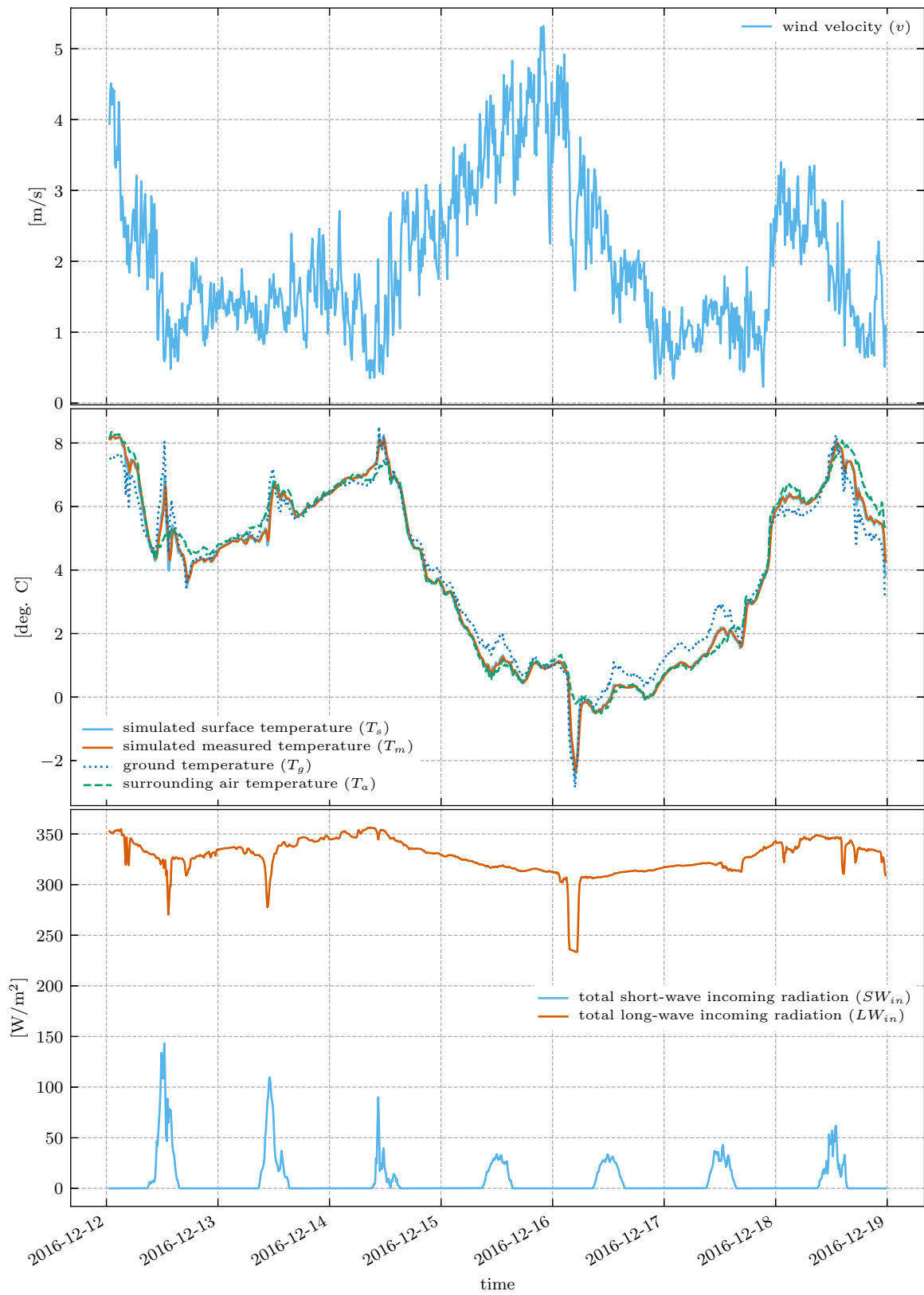
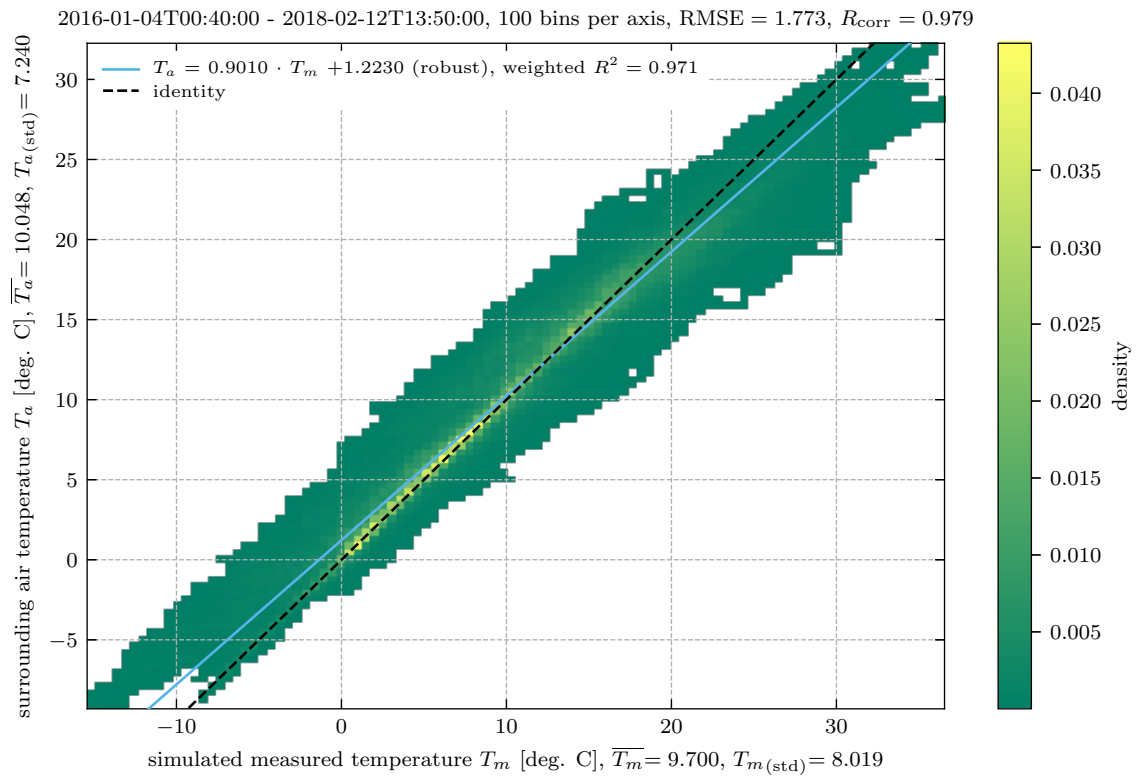
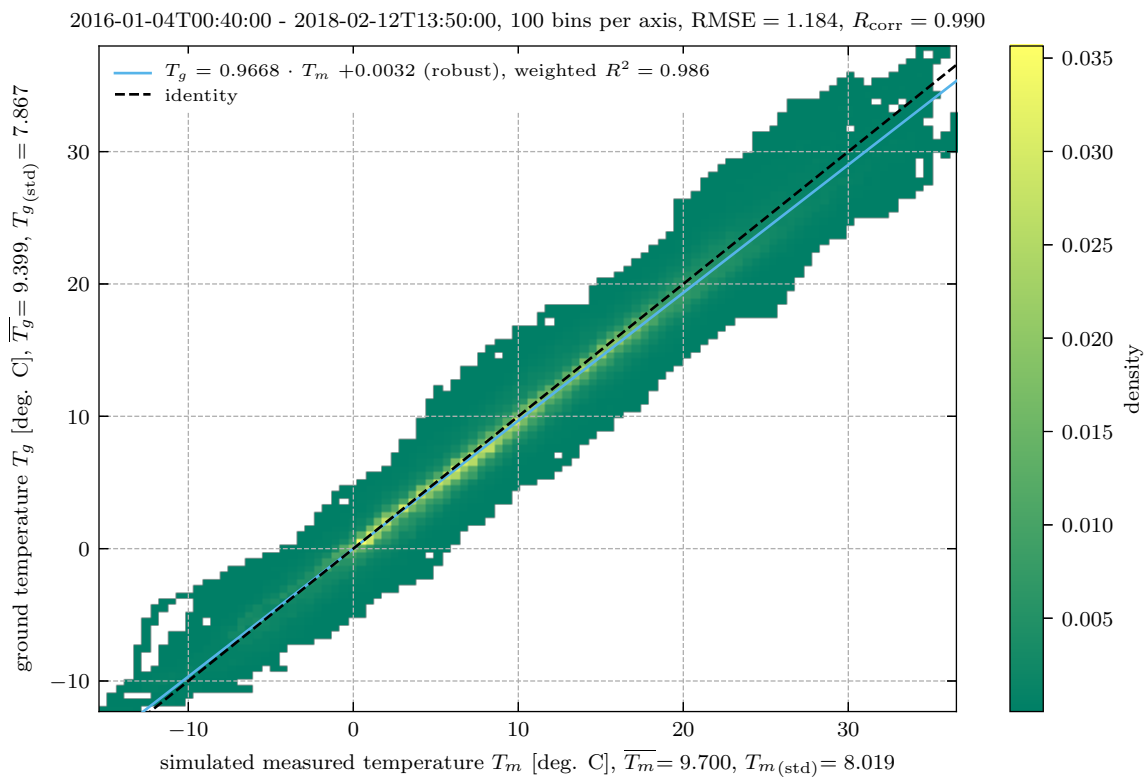


**Figure 5.3:** Simulated Netatmo outdoor module temperature alongside Wettermast HH forcing with original parameters (Table 4.3) during one winter week in 2016.



(a)



(b)

**Figure 5.4:** Wettermast HH air temperature (a) and ground surface temperature (b) vs. simulated Netatmo outdoor module temperature for the whole two-year reference simulation time span.

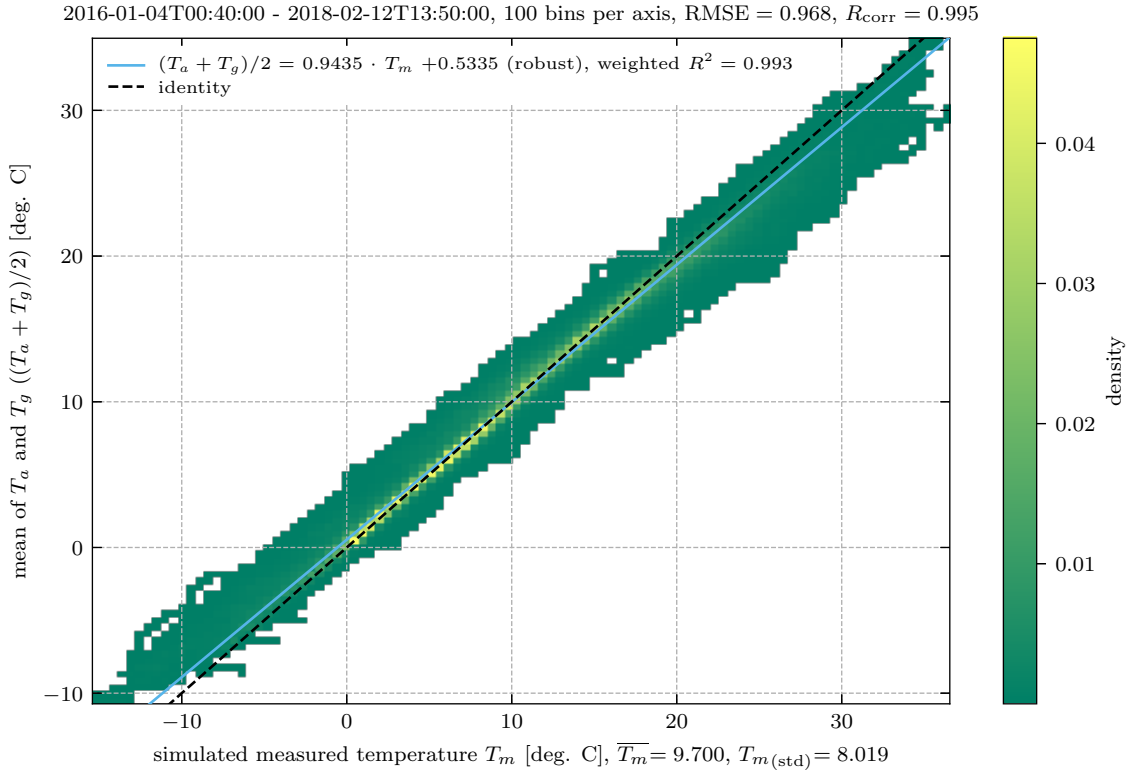
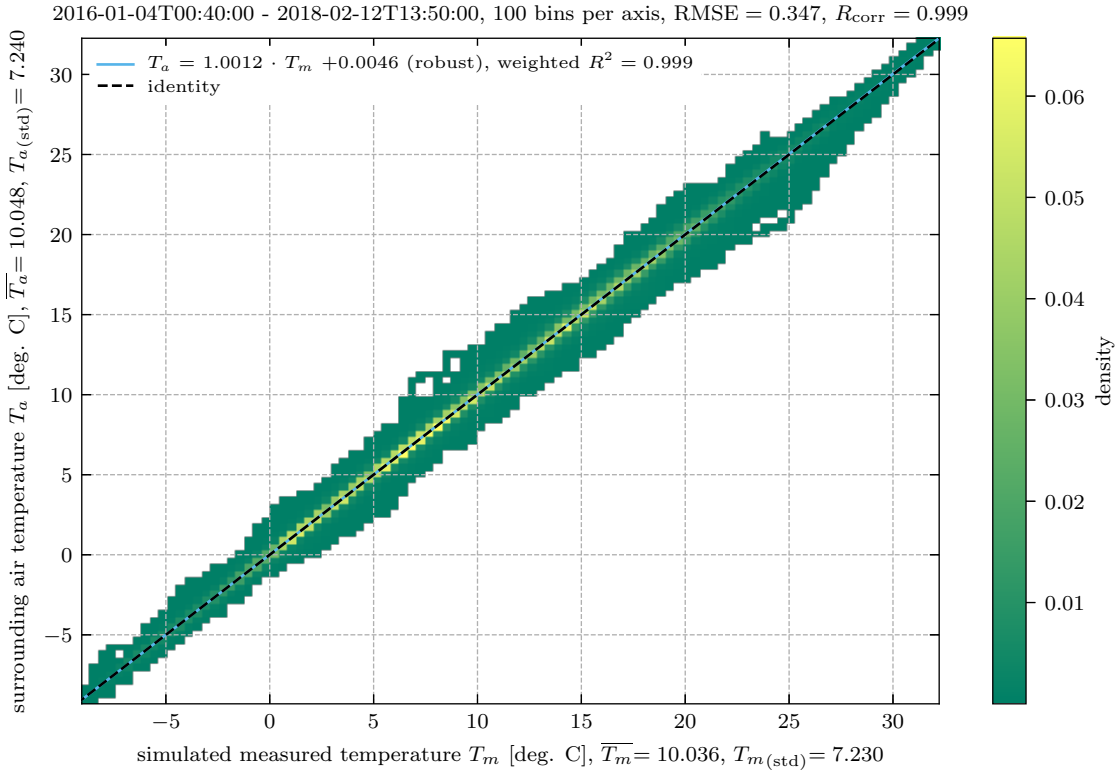


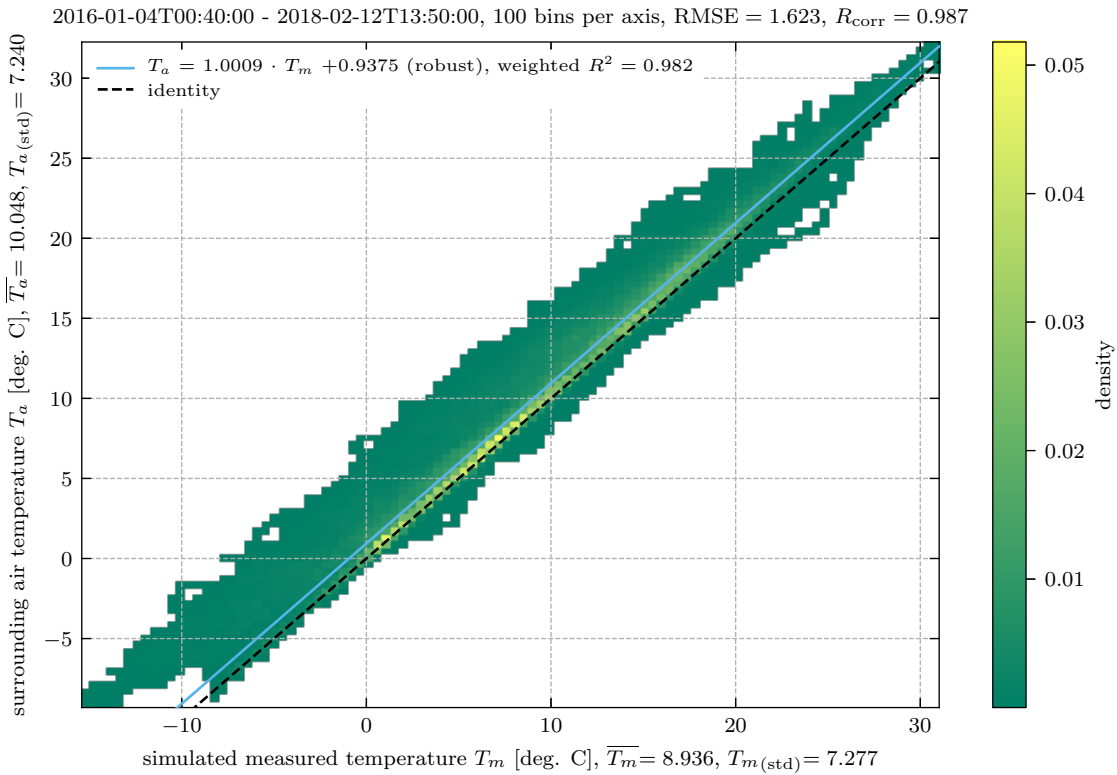
**Figure 5.5:** Simulated temperature vs. mean of Wettermast HH air and ground surface temperature with original parametrisation.

remaining physical processes influencing the outdoor module’s temperature measurement are the cover’s and sensor unit’s thermal inertia, the sensible and the latent heat flux. The latent heat flux has only very limited impact due to the coupling to the rather infrequent precipitation events. Thus, the dominant remaining process is the thermal inertia which is driven by the sensible heat flux. The simulation of this scenario features a substantially smaller RMSE of 0.35 K to the Wettermast HH air temperature (Figure 5.6a). This error is even in the order of magnitude of the SHT20 sensor chip’s accuracy (Section 2.2) and constitutes only 20 % of the total RMSE from the reference simulation in Figure 5.4a. Hence, the radiation budget definitely has the greatest influence on this simulated outdoor module’s temperature measurement compared to the other forcing. Since this result is so significant, this conclusion should also be applicable to real Netatmo outdoor module measurements.

If the cover is simulated to only reflect all short-wave radiation but still absorb and emit long-wave radiation ( $\alpha_s = 1$ ), the outdoor module’s temperature output becomes significantly colder (Figure 5.6b). The robust linear regression suggests a cold bias of 0.94 K to the forcing air temperature, which can be explained by the missing warming solar input. This also indicates that for an exposed Netatmo outdoor module the short-wave radiation is the dominant driver in air temperature overestimations.



(a)



(b)

**Figure 5.6:** Wettermast HH air temperature vs. simulated outdoor module temperature for (a) full reflective scenario ( $\alpha_s = 1$  and  $\varepsilon_s = 0$ ) and (b) only short-wave reflective scenario ( $\alpha_s = 1$ ).

## 5.4 Influence of the Outdoor Module Size

Another interesting question is the dependency of the outdoor module's temperature reading on its size. The only quantities in the energy balance equations Equation 3.14 and Equation 3.15 dependent on the outdoor module dimensions  $h_m$  and  $d_m$  are the areas  $A_r$  and  $A_s$  as well as the effective heat capacities  $C_s$  and  $C_m$ . The incoming short-wave radiation term includes the ratio of receiving and exposed surface area  $\frac{A_r}{A_s}$ . However, even when scaling both dimensions with a factor  $r$  (i.e.  $h_m' = r h_m$  and  $d_m' = r d_m$ ), this ratio stays the same:

$$\underbrace{\frac{A_r'}{A_s'}}_{\text{scaled ratio}} = \frac{r^2 d_m h_m}{\pi r^2 \left(\frac{d_m}{2}\right)^2 + \pi r^2 d_m h_m} = \frac{d_m h_m}{\pi \left(\frac{d_m}{2}\right)^2 + \pi d_m h_m} = \underbrace{\frac{A_r}{A_s}}_{\text{original ratio}} \quad (5.1)$$

With the parametrisation in use, this indicates that scaling the outdoor module's dimensions equally doesn't alter the influence of the short-wave radiation. The outdoor module's volume, however, is scaled with the third power of the scaling factor  $r$ :

$$V_m = h_m \pi \left(\frac{d_m}{2}\right)^2 \implies V_m' = r^3 h_m \pi \left(\frac{d_m}{2}\right)^2 \quad (5.2)$$

Assuming that the scaling keeps the overall cover and sensor unit density and material distribution constant, the heat capacities  $C_s$  and  $C_m$  are modified according to the change in volume. In conjunction with Equation 5.1 this follows that resizing the outdoor module while keeping its aspect ratio constant effectively only scales the thermal inertia terms for both cover and sensor unit with the scaling factor  $r$ :

$$\frac{C_s}{A_s} \frac{dT_s}{dt} \rightarrow r \frac{C_s}{A_s} \frac{dT_s}{dt} \quad \text{and} \quad \frac{C_m}{A_s} \frac{dT_i}{dt} \rightarrow r \frac{C_m}{A_s} \frac{dT_i}{dt} \quad (5.3)$$

According to this, an enlarged Netatmo outdoor module should simply have a greater time constant and react more slowly to environmental forcing changes, while a demagnified outdoor module should feature the opposite characteristics. A simulation of these scenarios for the same summer week as in Figure 5.2 is shown in Figure 5.8 ( $r = 2$ ) and Figure 5.9 ( $r = 0.5$ ).

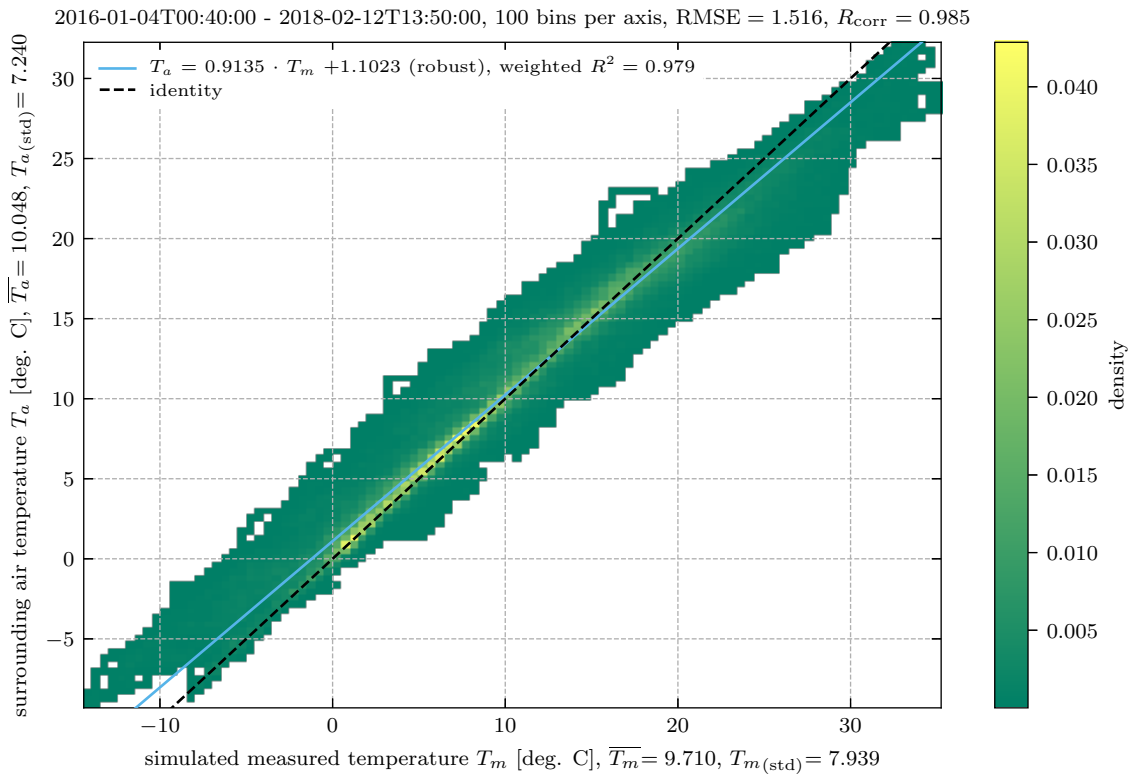
As expected, the enlarged scenario features a significantly smoother simulated outdoor module temperature. Furthermore, compared to the reference simulation in Figure 5.2, the simulated cover and sensor unit temperatures are more decoupled of each other. While the cover peaks multiple times a day, the sensor unit has at most two daily maxima of lower amplitude. In addition, the sensor unit's lag relating to the cover temperature is evident. On the contrary, the diminished scenario exhibits a much quicker response to any forcing variation. Both simulated reservoir temperatures are greatly alike as well in this case. However, the diminished scenario does not introduce fundamentally different features compared to the reference simulation.

The usual perception of air temperature probes is that a larger probe is generally more prone to radiative forcing and thus yields less reliable temperature readings (e.g. for thermocouples, see Campbell 1969). Interestingly, the results obtained from the simulations conducted in this section suggest the exact opposite conclusion. The virtually enlarged Netatmo outdoor module

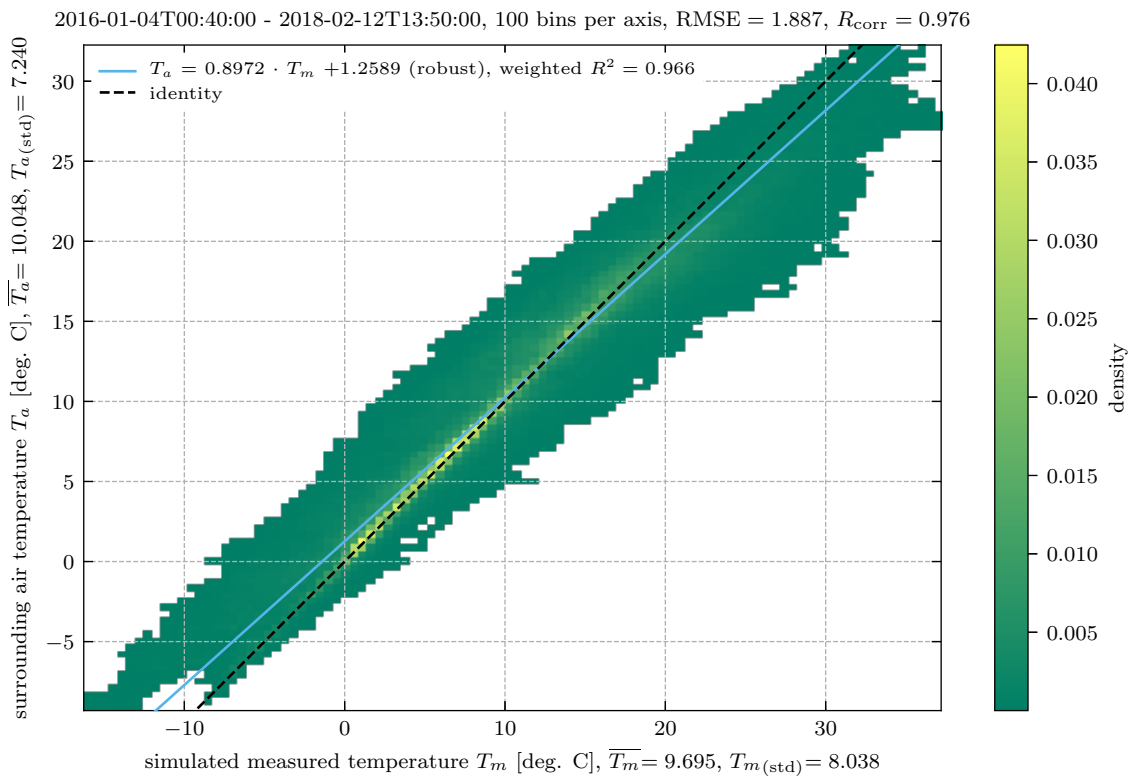
exhibits a greater consistency to the Wettermast HH air temperature than the reference simulation (0.26 K less RMSE between Figure 5.7a and Figure 5.4a) while the virtually diminished outdoor module has a greater error compared to the reference simulation (0.11 K increased RMSE between Figure 5.7b and Figure 5.4a).

This initially counterintuitive finding can be explained with the significant difference in thermal inertia between the Netatmo outdoor module and the probes examined by Campbell (1969), which all had small time constants ( $\tau < 2$  s). If the time constant, i.e. the thermal inertia, is very low, the reading becomes stationary more quickly because the thermal inertia term is negligibly small. On the contrary, probes with large thermal inertia react slower - the extreme example being a probe with infinite heat capacity that effectively has a constant temperature reading regardless of the forcing. The quality of an air temperature probe's measurement, e.g. quantified by the RMSE to the air temperature, depends heavily on both the probe's thermal inertia defining its reaction time and on the forcing itself. For example in a setup where the air temperature varies only moderately but the radiative forcing is still large, an infinitely slow probe would probably yield a lower error than a faster probe due to its resilience to radiative forcing. This effect is the reason for the conclusion that a virtually enlarged outdoor module yields simulated readings closer to the Wettermast HH air temperature than a diminished one. Due to its increased thermal inertia, the enlarged outdoor module does not reach the high amplitudes like the diminished outdoor module. Nevertheless, there will be a critical scaling factor  $r > 2$  above which the enlarged outdoor module simulation will yield temperature readings that are less in line with the forcing air temperature than the reference simulation.

Altogether it can be argued that the Netatmo outdoor module's size definitely has an influence on its measurement, but considering the large dimension scaling needed ( $r = 2$ ) to provoke a significant change in the characteristics, the conclusion is a rather small importance compared to other effects like the radiation budget. However, for a completely exposed Netatmo outdoor module, the dampening introduced by the greater thermal inertia when enlarging the outdoor module has a slightly positive effect on the quality of the air temperature measurement.



(a)



(b)

**Figure 5.7:** Wettermast HH air temperature vs. simulated Netatmo outdoor module temperature for a Netatmo outdoor module twice (a) and half (b) the original size.

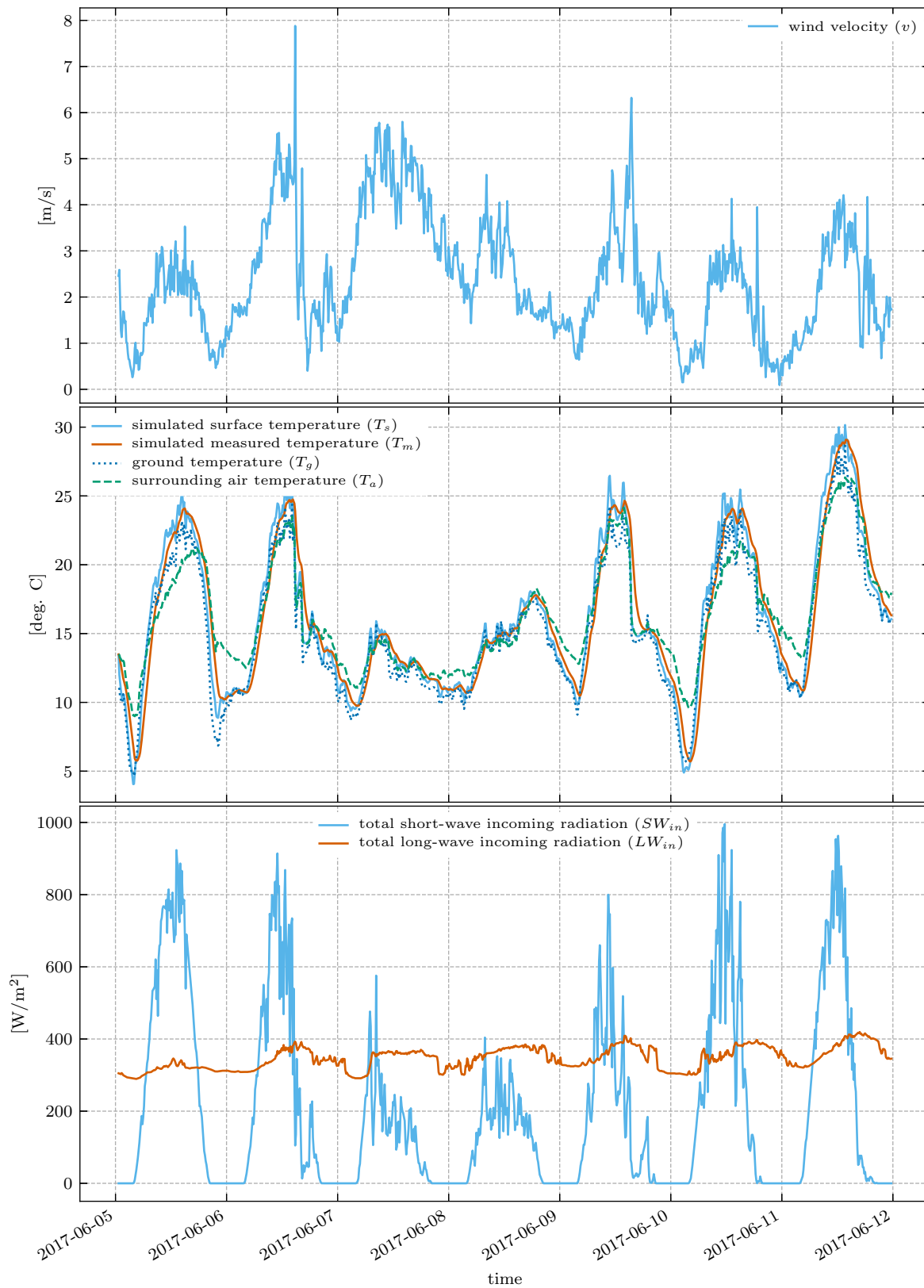


**Figure 5.8:** Simulated Netatmo outdoor module temperature alongside Wettermast HH air and ground surface temperature with a virtual outdoor module twice the original size ( $r = 2$ ) for the same summer week as in Figure 5.2

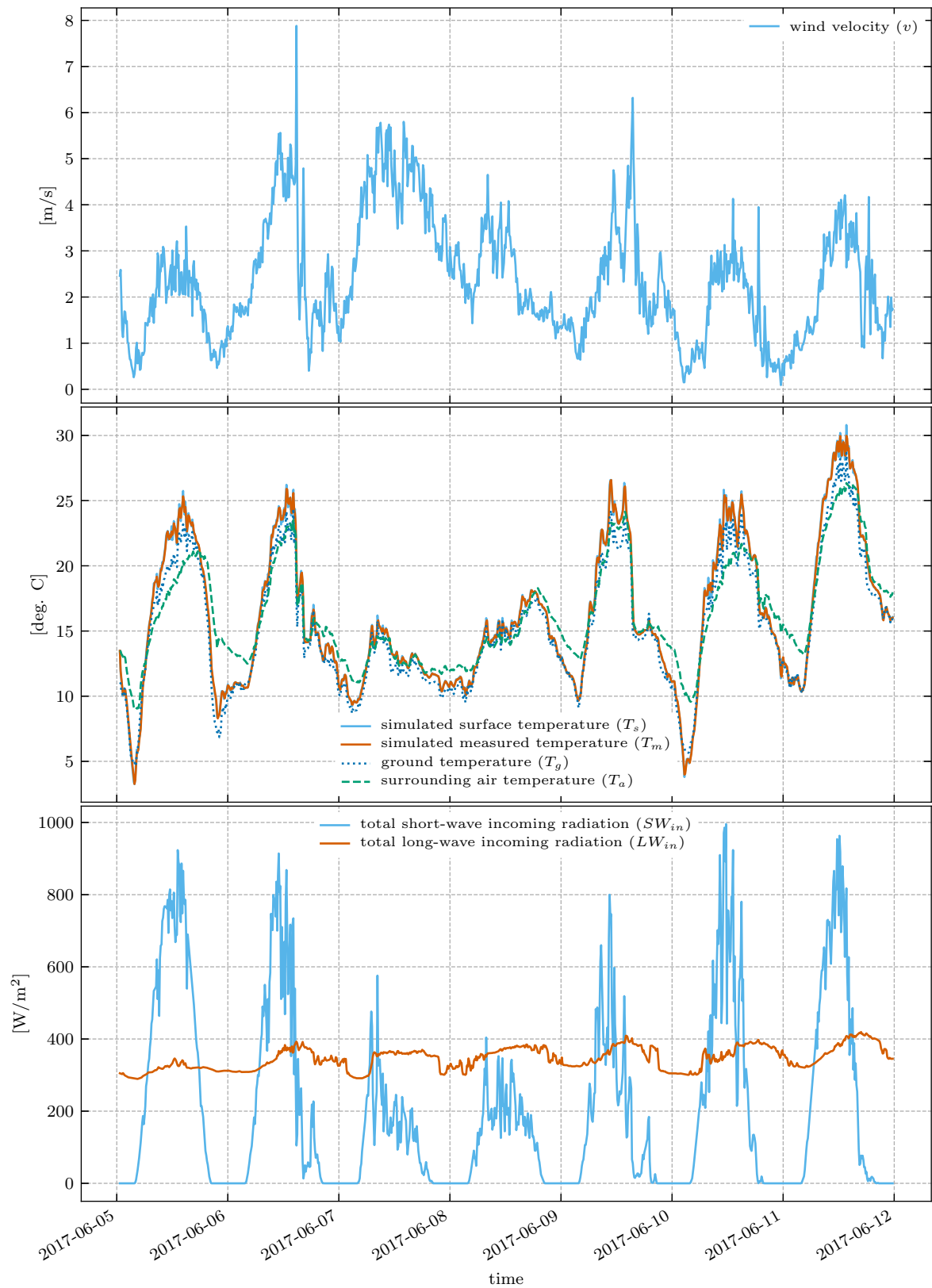


**Figure 5.9:** Simulated Netatmo outdoor module temperature alongside Wettermast HH air and ground surface temperature with a virtual outdoor module half the original size ( $r = 0.5$ ) for the same summer week as in Figure 5.2



# Chapter 6

## Conclusion

The present study assessed the temperature measurement process of the Netatmo outdoor module citizen weather station. Both experimental and simulative approaches were applied to obtain insights regarding the interpretation of a Netatmo outdoor module's temperature reading.

It was asserted experimentally that in a tested range of 18 °C to 42 °C, the embedded SENSIRION SHT20 temperature and humidity sensor chip is accurate to  $\pm 0.3$  K as stated in its specification. A conspicuously large time constant of more than 20 minutes was determined for the outdoor module in its normally assembled state under calm conditions. The time constant decreases to about 15 minutes if the Netatmo outdoor module's aluminium shell including the plastic inlet is removed.

To investigate the outdoor module's measurement characteristics quantitatively, a two-component energy balance model was then introduced. This model describes the outdoor module's cover separately from its sensor unit and connects both via heat conduction. The cover is assumed to be influenced by its radiation budget as well as sensible and latent heat fluxes. The model was calibrated using the classical approach of condensing the model equations and determining the parameters based on experimental data. Fine-tuning of the parameters was achieved by applying an optimization technique which improved the resimulation of the experimental data significantly.

Simulations of an exposed Netatmo outdoor module at the Wettermast Hamburg measurement site revealed several insights into its fundamental measurement characteristics. Generally, the simulated Netatmo outdoor module overestimates warm temperatures and underestimates colder temperatures. The overall RMSE between simulated outdoor module temperature and actual air temperature proved to be 1.77 K.

Above all, the short-wave radiation input stands out as the most significant cause of air temperature overestimation. In addition, the total radiation budget including the incoming and emitted long-wave radiation turned out to constitute the dominant driver of the simulated Netatmo outdoor module's temperature measurement in general. From this it appears that the simulated outdoor module rather measures a combination of both surrounding air and ground surface temperature instead of air temperature only. As a conclusion, real Netatmo outdoor module readings shouldn't be interpreted directly as air temperature but rather as a proxy for both air and surrounding building blackbody temperature in combination, e.g. a weighted average. The share of the surrounding blackbody temperature in this average is suggested to decrease with enhanced ventilation of the outdoor module.

Furthermore, simulations of Netatmo outdoor modules of different sizes were performed to assess the influence of its reaction time on the quality of the temperature reading. The finding of these simulations is that due to the increased resilience to strong forcing variations, a virtually enlarged outdoor module's reading is actually better in line with air temperature than a diminished one. Still, the effects are small. Altogether, the influence of the outdoor module's temporal lag on its temperature measurement is marginal compared to the influence of the radiation budget.



# Chapter 7

## Outlook

Several simplifying assumptions were made to keep the model at a reasonable level of complexity (Table 3.1). But as each assumption neglects specific actualities, the model has certain deficits, some of which were discussed above. This chapter elaborates on possible steps to improve the overall model quality and proposes another interesting method of applying this model.

### Calibration

First, the parameter calibration can be significantly improved by performing the parameter optimization (Section 4.2) based on real measurements instead of experiments conducted under laboratory conditions. For example, one or more Netatmo outdoor modules could be stationed at a professionally maintained site like the Wettermast Hamburg measurement site that provides measurements for all of the necessary forcing quantities (Table 3.2c).

### Calm Bulk Transfer Parameter

As detected in Figure 4.6, neglecting the sensible and latent heat flux under calm conditions as charted in Table 3.1VIII can cause an unclosed cover surface energy budget. This parametrisation could be enhanced by introducing a calm bulk transfer parameter  $\gamma$  that adds a sensible and latent flux term for wind-less conditions. Equation 3.9 and Equation 3.12 would then change to:

$$H_L = a_{\text{wet}} \rho_a L (q^*(T_s) - q_a) A_s (\gamma + \eta v) \quad (7.1)$$

$$H_S = \rho_a c_p (T_s - T_a) A_s (\gamma + \eta v) \quad (7.2)$$

A calm scenario (Table 4.1) then no longer neglects these heat fluxes. However, this conflicts with the calibration methods applied to determine the heat capacities  $C_s$  and  $C_m$  (Section 4.1). Hence, this improved parametrisation could be calibrated for example by an optimization.

### Latent Heat Flux

The latent heat flux parametrisation in Equation 3.12 was not quantified experimentally. Although the latent heat flux probably only has very limited influence on the overall cover energy balance, an experimentally calibrated parametrisation is still better.

## Bottom Heat Flux

The assumption in Table 3.1VI states that the heat flux through the bottom plate is ignored. As explained in Section 3.1, this is not ideal. As a first approximation for the temperature of the placing surface, the surrounding air temperature  $T_a$  could be used. The sensible heat flux into and from the placing surface could then be equally parametrised as the sensible heat flux to and from the surrounding air, only without the wind dependency. This would also further dampen the outdoor module's temperature reading, which might fit real outdoor module readings more adequately. Another option would be to parametrise the temperature of the placing surface in terms of ground surface temperature  $T_g$ .

## Short-Wave Input

The short-wave receiving surface area  $A_r$  is actually dependent on the sun's altitude because of the outdoor module's cylindrical shape. As the sun's altitude can easily be determined (Bretagnon and Francou 1988) depending on the time of the day, the short-wave receiving surface area could be parametrised using a simple cylinder geometry.

The incoming short-wave radiation parametrisation should also include a shadowing effect. To simulate arbitrary Netatmo outdoor modules in urban areas, an approach could be to assume that most outdoor modules in cities are placed on the balcony which in turn is most likely to point south. With a dataset of building heights, a shadowing parametrisation could be derived.

## Prognostic Equation for Wet Area Coverage

In Chapter 5, the cover's wet area coverage  $a_{\text{wet}}$  was parametrised very rudimentary in terms of a dichotomous precipitation detection signal. However, it is possible to develop a prognostic equation for the surface's wet area coverage  $a_{\text{wet}}$  based on the continuity of mass. The kinematic moisture flux on the cover's surface could be parametrised similarly to the latent heat flux (Wallace and Hobbs 2006):

$$F_w = \eta v (q_s - q_a) A_s \quad (7.3)$$

Adding the calm bulk transfer parameter  $\gamma$  yields:

$$F_w = (\gamma + \eta v) (q_s - q_a) A_s \quad (7.4)$$

Then, the maximum amount of liquid water that the cover can hold needs to be determined experimentally, e.g. by moisturising the cover, wiping the water up and weighing it. The equation for the continuity of mass would then consist of the moisture flux and a forcing term that increases the mass of water in terms of precipitation.

## Inverse Modelling

A very interesting case of model application is the method of inverse modelling (Figure 7.1). Simulating the Netatmo outdoor module's temperature reading given the environmental forcing can be termed as the concept of forward modelling. However, while this method is appropriate to examine the characteristics of a system, it is not suitable to manipulate real Netatmo outdoor module readings. Inverse modelling can be used to retrace the forcing from given outdoor module readings. This is achieved by optimizing the forcing as explained in Figure 4.7 and defining the reference state as the temperature measurement of an arbitrary outdoor module. In principle, this inverse modelling technique could then be used to extract the ambient air temperature or even the short-wave radiation that this outdoor module receives from its temperature reading. Still, this requires the model to be precisely calibrated.

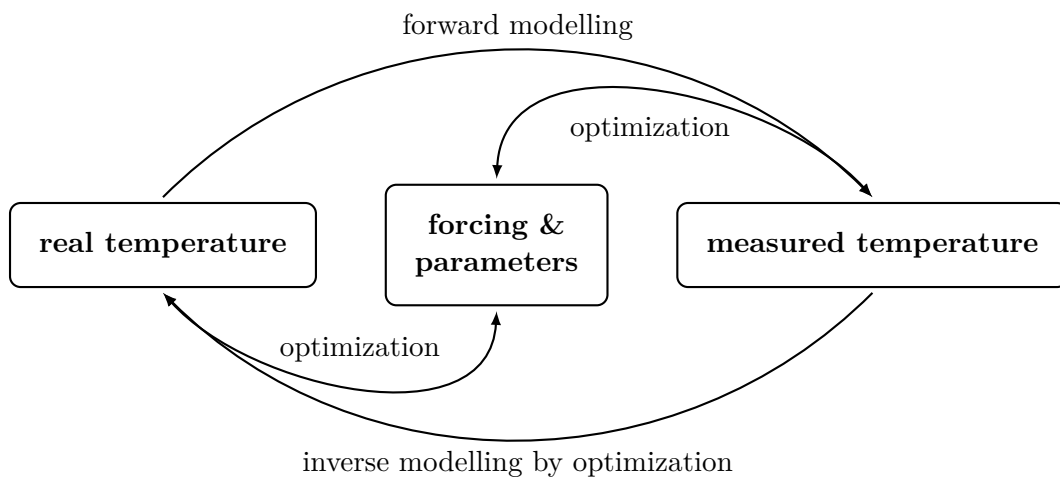


**Figure 7.1:** Inverse modelling concept



# References

- Bell, Simon, Dan Cornford and Lucy Bastin (2015). ‘How good are citizen weather stations? Addressing a biased opinion’. In: *Weather* 70.3, pp. 75–84.
- Bretagnon, Pierre and Gérard Francou (1988). ‘Planetary theories in rectangular and spherical variables-VSOP 87 solutions’. In: *Astronomy and Astrophysics* 202, pp. 309–315.
- Bröring, Arne, Albert Remke and Damian Lasnia (2011). ‘SenseBox—a generic sensor platform for the web of things’. In: *International Conference on Mobile and Ubiquitous Systems: Computing, Networking, and Services*. Springer, pp. 186–196.
- Brümmer, Burghard, Ingo Lange and Heike Konow (2012). ‘Atmospheric boundary layer measurements at the 280 m high Hamburg weather mast 1995–2011: mean annual and diurnal cycles’. In: *Meteorologische Zeitschrift* 21.4, pp. 319–335.
- Bruns, Julian et al. (2018). ‘Automated Quality Assessment of (Citizen) Weather Stations’. In: *arXiv preprint arXiv:1802.06018*.
- Büchau, Yann (2017a). *numericalmodel: set up and run simple numerical models in Python*. Version 0.1.19. [Online; accessed 12<sup>th</sup> January, 2018]. URL: <https://pypi.python.org/pypi/numericalmodel>.
- (2017b). *patatmo: painless access to the Netatmo weather API*. Version 0.2.14. [Online; accessed 12<sup>th</sup> January, 2018]. URL: <https://pypi.python.org/pypi/patatmo>.
- Byrd, Richard H et al. (1995). ‘A limited memory algorithm for bound constrained optimization’. In: *SIAM Journal on Scientific Computing* 16.5, pp. 1190–1208.
- Campbell, GS (1969). *Measurement of air temperature fluctuations with thermocouples*. Tech. rep. Army Electronics Command White Sands Missile Range Nm Atmospheric Sciences Lab.
- Chapman, Lee (2015). ‘Urban meteorological networks: an urban climatologists panacea’. In: *9th International Conference on Urban Climate (IAUC & AMS), open plenary speech*, pp. 20–24.
- Chapman, Lee, Cassandra Bell and Simon Bell (2017). ‘Can the crowdsourcing data paradigm take atmospheric science to a new level? A case study of the urban heat island of London quantified using Netatmo weather stations’. In: *International Journal of Climatology* 37.9, pp. 3597–3605.
- Chauvin, Rémi et al. (2015). ‘Modelling the clear-sky intensity distribution using a sky imager’. In: *Solar Energy* 119, pp. 1–17.
- Dormand, John R and Peter J Prince (1980). ‘A family of embedded Runge-Kutta formulae’. In: *Journal of computational and applied mathematics* 6.1, pp. 19–26.
- Eliasson, I and MK Svensson (2003). ‘Spatial air temperature variations and urban land use—a statistical approach’. In: *Meteorological Applications* 10.2, pp. 135–149.
- Fenner, Daniel et al. (2014). ‘Spatial and temporal air temperature variability in Berlin, Germany, during the years 2001–2010’. In: *Urban Climate* 10, pp. 308–331.
- Fofonoff, Nick P, SP Hayes and Robert C Millard (1974). *WHOI/Brown CTD microprofiler: methods of calibration and data handling*. Tech. rep. Woods Hole Oceanographic Institution.
- Fraedrich, Klaus (2001). ‘Simple climate models’. In: *Progress in Probability* 49, pp. 65–110.
- Gershenfeld, Neil, Raffi Krikorian and Danny Cohen (2004). ‘The internet of things’. In: *Scientific American* 291.4, pp. 76–81.

- Gilchrist, Glen (2011). *A simple method to determine surface albedo using digital photography*. [Online; accessed 27<sup>th</sup> January, 2018]. URL: <http://vixra.org/pdf/1110.0035v1.pdf>.
- Gryning, Sven-Erik et al. (2014). ‘Long-term profiles of wind and Weibull distribution parameters up to 600 m in a rural coastal and an inland suburban area’. In: *Boundary-layer meteorology* 150.2, pp. 167–184.
- Guinard, Dominique and Vlad Trifa (2009). ‘Towards the web of things: Web mashups for embedded devices’. In: *Workshop on Mashups, Enterprise Mashups and Lightweight Composition on the Web (MEM 2009), in proceedings of WWW (International World Wide Web Conferences), Madrid, Spain*. Vol. 15.
- Haddad, Richard A and Thomas W Parsons (1991). *Digital signal processing: theory, applications, and hardware*. Computer Science Press, Inc.
- Horne, EPW and JM Toole (1980). ‘Sensor response mismatches and lag correction techniques for temperature-salinity profilers’. In: *Journal of Physical Oceanography* 10.7, pp. 1122–1130.
- Houghton, John T et al. (1997). *An introduction to simple climate models used in the IPCC Second Assessment Report*. WMO; UNEP.
- Huber, Peter J (1964). ‘Robust estimation of a location parameter’. In: *The annals of mathematical statistics*, pp. 73–101.
- ITU Radiocommunication Assembly (1995). *Studio encoding parameters of digital television for standard 4: 3 and wide-screen 16: 9 aspect ratios*.
- Jones, Eric, Travis Oliphant, Pearu Peterson et al. (2001). *SciPy: Open source scientific tools for Python*. [Online; accessed 16<sup>th</sup> January, 2018]. URL: <http://www.scipy.org/>.
- Kim, Yeon-Hee and Jong-Jin Baik (2005). ‘Spatial and temporal structure of the urban heat island in Seoul’. In: *Journal of Applied Meteorology* 44.5, pp. 591–605.
- Kurtz, Benjamin and Jan Kleissl (2017). ‘Measuring diffuse, direct, and global irradiance using a sky imager’. In: *Solar Energy* 141, pp. 311–322.
- Lundquist, Jessica D and Brian Huggett (2008). ‘Evergreen trees as inexpensive radiation shields for temperature sensors’. In: *Water resources research* 44.4.
- Meier, Fred et al. (2015). ‘Challenges and benefits from crowd sourced atmospheric data for urban climate research using Berlin, Germany, as testbed’. In: *ICUC9–9th International Conference on Urban Climate jointly with 12th Symposium on the Urban Environment*.
- Meier, Fred et al. (2017). ‘Crowdsourcing air temperature from citizen weather stations for urban climate research’. In: *Urban Climate* 19, pp. 170–191.
- Miloshevich, Larry M et al. (2004). ‘Development and validation of a time-lag correction for Vaisala radiosonde humidity measurements’. In: *Journal of Atmospheric and Oceanic Technology* 21.9, pp. 1305–1327.
- Muller, CL et al. (2015). ‘Crowdsourcing for climate and atmospheric sciences: current status and future potential’. In: *International Journal of Climatology* 35.11, pp. 3185–3203.
- Nakamura, Reina and L Mahrt (2005). ‘Air temperature measurement errors in naturally ventilated radiation shields’. In: *Journal of Atmospheric and Oceanic Technology* 22.7, pp. 1046–1058.
- Netatmo SAS (2018a). *company website*. [Online; accessed 10<sup>th</sup> January, 2018]. URL: <https://netatmo.com>.
- (2018b). *Netatmo Connect API Reference*. [Online; accessed 8<sup>th</sup> January, 2018]. URL: <https://dev.netatmo.com/resources>.

- Netatmo SAS (2018c). *Netatmo Weathermap*. [Online; accessed 6<sup>th</sup> January, 2018]. URL: <https://weathermap.netatmo.com>.
- Nocedal, Jorge and Stephen Wright (2000). *Numerical Optimization (Springer Series in Operations Research and Financial Engineering)*. Springer.
- North, Gerald R, Robert F Cahalan and James A Coakley (1981). ‘Energy balance climate models’. In: *Reviews of Geophysics* 19.1, pp. 91–121.
- Payne, Richard E (1972). ‘Albedo of the sea surface’. In: *Journal of the Atmospheric Sciences* 29.5, pp. 959–970.
- Rossini, Elton G and Arno Krenzinger (2007). ‘Maps of sky relative radiance and luminance distributions acquired with a monochromatic CCD camera’. In: *Solar Energy* 81.11, pp. 1323–1332.
- Sensirion (2014). *Datasheet SHT20 - Humidity and Temperature Sensor IC*. [Online; accessed 2<sup>nd</sup> February, 2018]. URL: [https://www.sensirion.com/fileadmin/user\\_upload/customers/sensirion/Dokumente/2\\_Humidity\\_Sensors/Sensirion\\_Humidity\\_Sensors\\_SHT20\\_Datasheet.pdf](https://www.sensirion.com/fileadmin/user_upload/customers/sensirion/Dokumente/2_Humidity_Sensors/Sensirion_Humidity_Sensors_SHT20_Datasheet.pdf).
- Speight, James G et al. (2005). *Lange’s handbook of chemistry*. Vol. 1. McGraw-Hill New York.
- Wallace, John M and Peter V Hobbs (2006). *Atmospheric science: an introductory survey*. Vol. 92. Academic press.
- Watson, Andrew B, Quingmin J Hu and John F McGowan (2001). ‘Digital video quality metric based on human vision’. In: *Journal of Electronic imaging* 10.1, pp. 20–30.
- Weast, Robert C (1981). *CRC Handbook of Chemistry and Physics 62nd Edition 1981-1982*. CRC PRESS INC @.
- Zhu, Ciyou et al. (1997). ‘Algorithm 778: L-BFGS-B: Fortran subroutines for large-scale bound-constrained optimization’. In: *ACM Transactions on Mathematical Software (TOMS)* 23.4, pp. 550–560.



# Acknowledgements

This study was very instructive for me. I learned a lot about modelling and measuring in general and I would like to thank several individuals who have all helped me throughout the process in various ways.

Above all, I would like to thank Prof. Dr. Felix Ament for motivating this interesting topic and making this study possible at all. In every discussion with him - no matter the duration - I received very valuable scientific input which always helped getting along better. Furthermore, I am thankful for his efforts in bringing me in touch with Dr. Fred Meier from the Department of Ecology at the Technical University of Berlin, whom I am grateful for the collaboration.

I would also like to thank Dr. Sarah Wiesner for all the support she gave. Especially the advice for improving the language of this work was very helpful. At any time she was willing to hear and comment my elaborations. Moreover, I really appreciate her impulse mobilising me to attend the MyKlima Colloquium - thanks to Dr. Benjamin Bechtel for the invitation - and the DKG (German Congress of Geography) to present my current research state. Both were very interesting and inspiring events.

I am also especially grateful for Rainer Senke's extensive technical support. Whenever I had questions concerning soldering, tools or electronics in general, he was instantly ready to help me overcome my technical problems. His vast knowledge of anything electronic and beyond made conversations with him supremely interesting, informative and fun.

Furthermore, I would like to thank Michael Offermann for his technical assistance with the meteorological devices I used throughout the study. He also pointed me into the right direction of determining the cover albedo by proposing to use an old reflex camera.

Then, I am thankful for all of Ingo Lange's diverse assistance. When one is stuck, one can always count on his unparalleled knowledge and pragmatic handling of meteorological measurements. He had the brilliant idea of letting the climate chamber cool down slowly to obtain comparable time series of the HMP and the Netatmo outdoor modules and always had an ear for my work. I would also like to thank the SciPy community (Jones et al. 2001) for providing such an outstanding framework for scientific computing in Python.

Eventually, I am very grateful for all the support that my family is giving me.

Thank You!





# Versicherung An Eides Statt

Hiermit versichere ich an Eides statt, dass ich die vorliegende Arbeit im Studiengang Meteorologie selbstständig verfasst und keine anderen als die angegebenen Hilfsmittel – insbesondere keine im Quellenverzeichnis nicht benannten Internet-Quellen – benutzt habe. Alle Stellen, die wörtlich oder sinngemäß aus Veröffentlichungen entnommen wurden, sind als solche kenntlich gemacht. Ich versichere weiterhin, dass ich die Arbeit vorher nicht in einem anderen Prüfungsverfahren eingereicht habe und die eingereichte schriftliche Fassung der auf dem elektronischen Speichermedium entspricht.

(Yann Georg Büchau)

Hamburg, den 13. März 2018

